JGR Oceans

RESEARCH ARTICLE
10.1029/2019JC015261

Characteristics and Transformation of Pacific Winter Water on the Chukchi Sea Shelf in Late Spring

Astrid Pacini[1,2], G. W. K. Moore[3], Robert S. Pickart[1], Carolina Nobre[1], Frank Bahr[1], Kjetil Våge[4], and Kevin R. Arrigo[5]

[1]Woods Hole Oceanographic Institution, Woods Hole, MA, USA, [2]MIT-WHOI Joint Program in Physical Oceanography, Woods Hole, MA, USA, [3]Department of Physics, University of Toronto, Toronto, Ontario, Canada, [4]Geophysical Institute, University of Bergen and Bjerknes Centre for Climate Research, Bergen, Norway, [5]Department of Earth System Science, Stanford University, Stanford, CA, USA

Key Points:

1. Newly ventilated Pacific-origin winter water, with high nutrient content, is prevalent across the Chukchi Sea shelf in late spring.
2. A polynya model, used with a 1D mixing model, demonstrates that brine rejection from refreezing leads quickly overturns the water column.
3. Salinity signals and ice concentration data support the notion that winter water is modified within small leads throughout the shelf.

Correspondence to:
A. Pacini,
apacini@whoi.edu

Citation:
Pacini, A., Moore, G. W. K., Pickart, R. S., Nobre, C., Bahr, F., Våge, K., & Arrigo, K. R. (2019). Characteristics and transformation of Pacific winter water on the Chukchi Sea shelf in late-spring. *Journal of Geophysical Research: Oceans*, *124*, 7153–7177. https://doi.org/10.1029/2019JC015261

Received 3 MAY 2019
Accepted 17 SEP 2019
Accepted article online 14 Oct 2019
Published online 24 Oct 2019

Abstract Data from a late spring survey of the northeast Chukchi Sea are used to investigate various aspects of newly ventilated winter water (NVWW). More than 96% of the water sampled on the shelf was NVWW, the saltiest (densest) of which tended to be in the main flow pathways on the shelf. Nearly all of the hydrographic profiles on the shelf displayed a two-layer structure, with a surface mixed layer and bottom boundary layer separated by a weak density interface (on the order of 0.02 kg/m^3). Using a polynya model to drive a one-dimensional mixing model, it was demonstrated that, on average, the profiles would become completely homogenized within 14–25 hr when subjected to the March and April heat fluxes. A subset of the profiles would become homogenized when subjected to the May heat fluxes. Since the study domain contained numerous leads within the pack ice—many of them refreezing—and since some of the measured profiles were vertically uniform in density, this suggests that NVWW is formed throughout the Chukchi shelf via convection within small openings in the ice. This is consistent with the result that the salinity signals of the NVWW along the central shelf pathway cannot be explained solely by advection from Bering Strait or via modification within large polynyas. The local convection would be expected to stir nutrients into the water column from the sediments, which explains the high nitrate concentrations observed throughout the shelf. This provides a favorable initial condition for phytoplankton growth on the Chukchi shelf.

Plain Language Summary Shipboard data from a rare late spring cruise to the Chukchi Sea, in May–June 2014, are analyzed in order to understand the physical conditions of the waters on the shelf. More than 95% of the water on the shelf was very cold, high-nutrient winter water. The vertical structure of the water column (in temperature, salinity, and density) consisted of two layers, a well-mixed surface layer and a bottom boundary layer, separated by a weak density interface. When ice is formed at the surface, brine is rejected into the water column, densifying the surface water. This leads to convective overturning as dense water sinks and mixes with the subsurface water. If enough brine is rejected, the density interface between the mixed layers can be eroded and the water column mixes to the bottom, resulting in a uniform density profile. Nutrients are then stirred into the water column from the sediments, which preconditions the water for phytoplankton growth. Using realistic atmospheric conditions, together with a polynya model and ocean mixing model, it was demonstrated that this process was likely happening within small openings in the sea ice throughout the domain. This represents a new paradigm for forming winter water on the Chukchi shelf.

1. Introduction

The cold and dense winter water that flows northward through the Chukchi Sea each year is critical to the functioning of the regional ecosystem. The high nutrient content of the water spurs primary production on the shelf. When the pack-ice first retreats, open water phytoplankton blooms develop, which utilize the nutrients (e.g., Hill & Cota, 2005). Furthermore, it has recently been determined that earlier in the season, under-ice phytoplankton blooms can also form on the Chukchi shelf if enough sunlight is able to penetrate the first-year ice (Arrigo et al., 2014; Lowry et al., 2014). As the nutrients are drawn down during the spring and summer, these blooms deepen in the water column, dictated by the location of the nutricline—which in turn is largely determined by the presence of the winter water (Lowry et al., 2015, 2018).

The dense winter water is also of central importance for the maintenance of the halocline in the Canada Basin. After exiting the Chukchi shelf, much of the water is fluxed into the basin via turbulent processes.

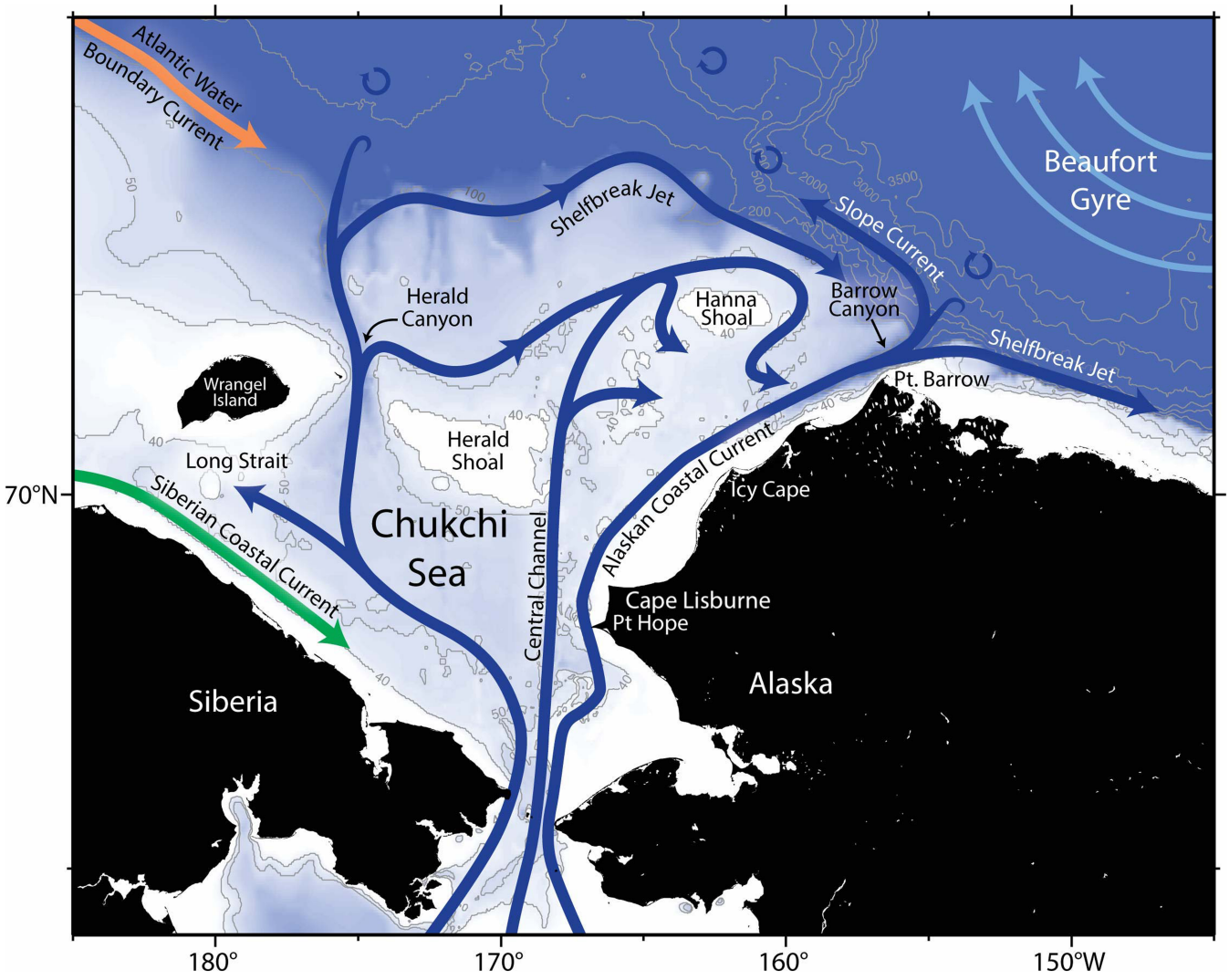

Figure 1. Schematic circulation of the Chukchi Sea (after Corlett & Pickart, 2017 and Li et al., 2019) and geographical place names.

In particular, the two shelfbreak jets that transport the winter water along the edges of the Chukchi and Beaufort Seas, respectively, are baroclinically unstable and spawn eddies, which carry the water seaward (Pickart et al., 2005; Spall et al., 2008; von Appen & Pickart, 2012). Cold-core anticyclonic eddies populate the Canada Basin (Timmermans et al., 2008) and are the most commonly observed type of eddy in the western arctic (Zhao et al., 2014). Their occurrence in the Canada Basin has been increasing in recent years (Zhao et al., 2016). As these features spin down, they influence the basin-scale stratification of the halocline, which is critical because this limits the vertical heat flux from the warm Atlantic layer below (that would otherwise melt the pack-ice). Recently, it has been shown that a significant amount of the water exiting the Chukchi shelf through Barrow Canyon forms a westward-flowing current along the continental slope of the Chukchi Sea (Corlett & Pickart, 2017; Li et al., 2019, see Figure 1). This may be another effective mechanism for transporting winter water into the basin.

Because of the overall dearth of observations in the Chukchi Sea during the cold months of the year, relatively little is known about the formation, modification, and circulation of winter water on the shelf. It is documented that such cold and dense water is formed in the northern Bering Sea (e.g., Muench et al., 1988), which then flows northward through Bering Strait from roughly January through April (Woodgate et al., 2005). Hence, there is a steady supply of winter water to the Chukchi Sea from the south. However, the degree to which the water is altered as it progresses across the shelf is not well-documented. Year-long mooring

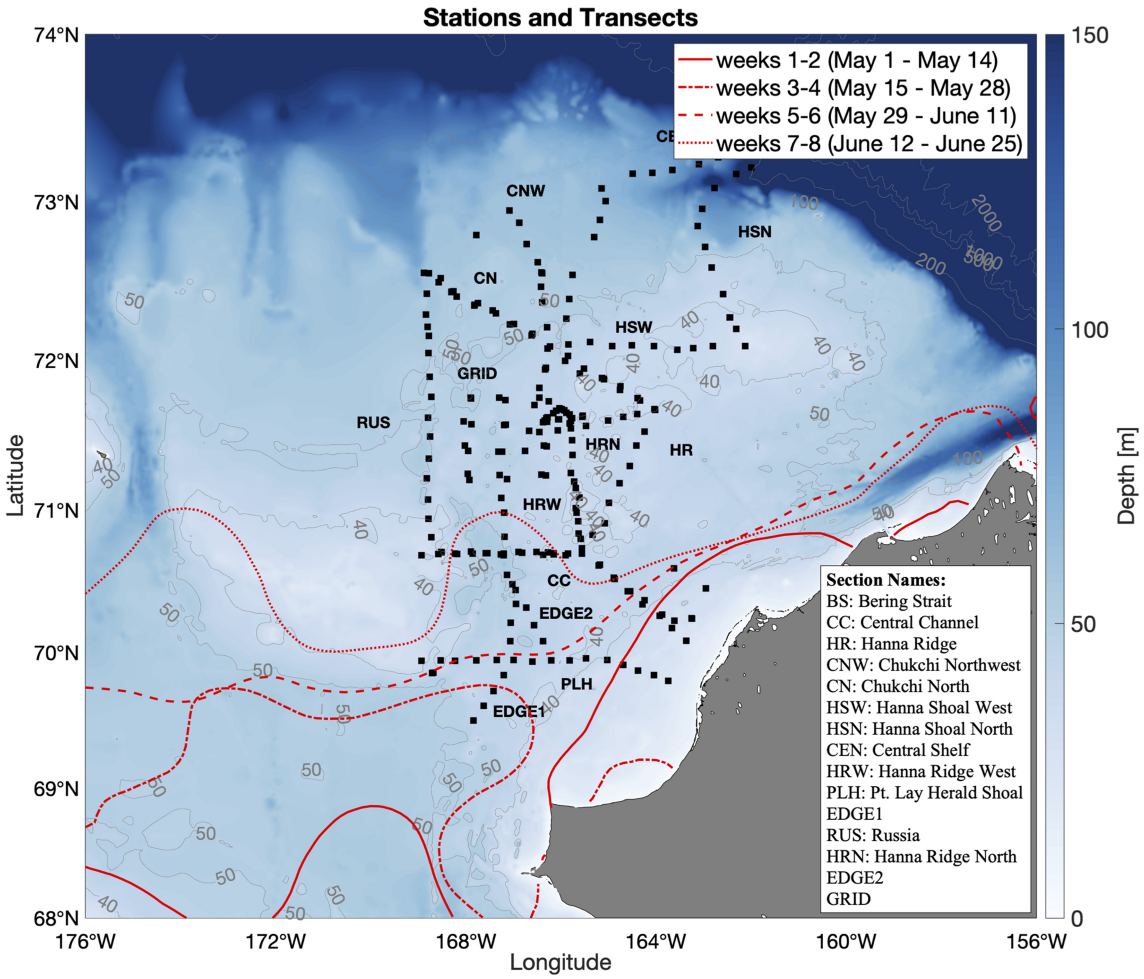

Figure 2. Locations of the hydrographic stations occupied on the 2014 cruise. See the legend for transect names. The Bering Strait line that was occupied is not considered in this study. The bathymetry is from IBCAO version 3. The red lines indicate the mean location of the 80% ice concentration edge every 2 weeks during the survey (slightly smoothed). The ice concentration data come from the AMSR-2 product (Beitsch et al., 2014).

records from select areas on the shelf have demonstrated that the winter water can be further densified within large polynyas. In particular, refreezing within the northeast Chukchi polynya can produce a very salty and dense product known as hypersaline winter water (Gong & Pickart, 2016; Itoh et al., 2012; Weingartner et al., 1998). It has also been shown that the degree of modification within this polynya varies from year to year (Itoh et al., 2012). However, it is currently unknown if modification of winter water takes place throughout the central Chukchi shelf and if smaller leads (versus large polynyas) play a role.

The transport of Pacific water from Bering Strait through the Chukchi Sea occurs along three main pathways (Figure 1): via Hope Valley in the west (Weingartner et al., 1998), via the Central Channel (Weingartner et al., 2005), and via the Alaskan Coastal Current in the east (Paquette & Bourke, 1974). There is increasing evidence, however, that the flow is not nearly as rigidly set along these three distinct pathways as was originally thought. In particular, it is now known that a portion of the western branch veers eastward to the north of Herald Shoal and joins the central branch (Pickart et al., 2010, 2016). Also, as the water approaches Hanna Shoal, it appears to split into two branches that progress around both sides of the shoal, subsequently dividing into even smaller filaments (Pickart et al., 2016). Sparsely placed moorings on the shelf have documented that winter water flows along the main pathways during winter and spring (e.g. Weingartner et al., 2005; Woodgate et al., 2005). Furthermore, hydrographic surveys have revealed that winter water is still present within the pathways on the northern portion of the shelf in the early summer (Gong & Pickart, 2016; Pickart et al., 2016) and exiting the shelf via Barrow Canyon in late summer (Pickart et al., 2019).

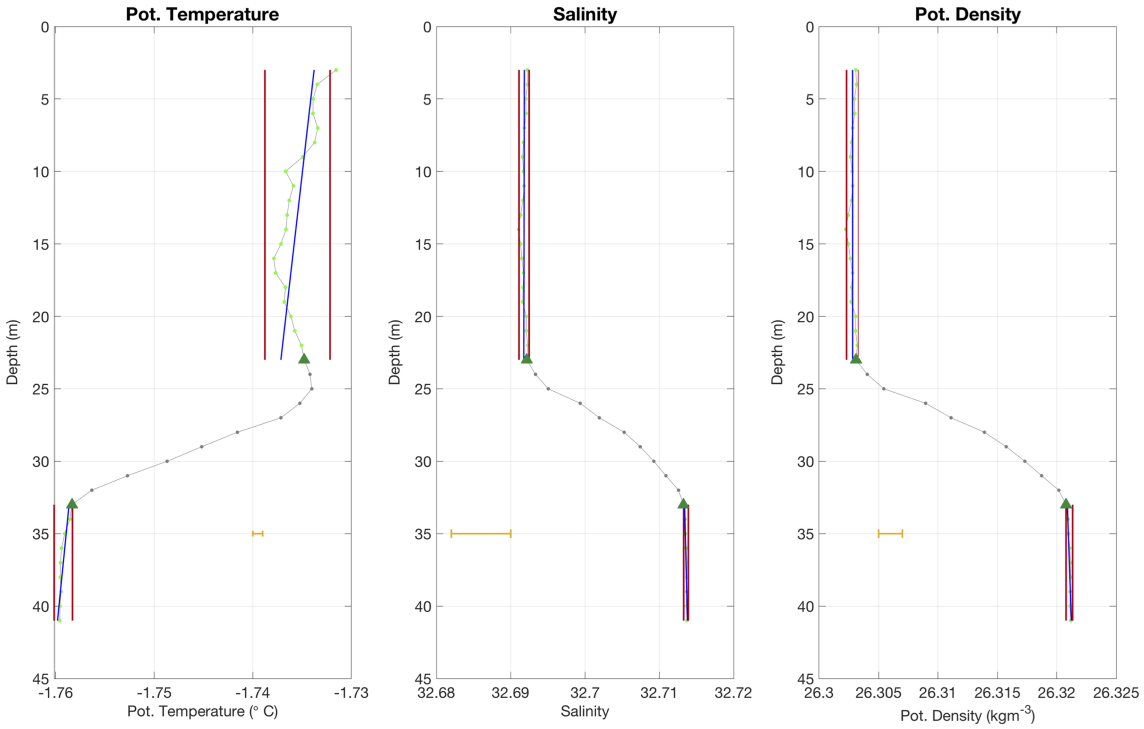

Figure 3. Vertical profiles of (a) potential temperature, (b) salinity, and (c) potential density for a typical conductivity-temperature-depth station containing newly ventilated winter water. The bottom of the surface mixed layer and the top of the bottom mixed layer are denoted by green triangles. The red lines denote the two standard deviation envelope used to identify the mixed layers, and the blue lines are the regression lines (see text). The yellow bars denote the precision of the conductivity-temperature-depth sensors.

However, the extent to which the cold water is present outside of these pathways—prior to summer—has yet to be determined.

In this study, we use data from a late spring, broad-scale survey of the northeast Chukchi Sea to investigate the distribution and characteristics of winter water on the shelf. We demonstrate that winter water was prevalent throughout the study region—both within the main flow pathways and outside of them. The data reveal that the density structure of the shelf during this time of year can be characterized as a two-layer system, and we investigate various aspects of this. In addition, we assess the ability of the water column to be homogenized into a single layer within leads due to atmospheric forcing, which modifies the winter water by salinizing it through sea ice formation and brine rejection.

The structure of the paper is as follows. We begin with a presentation of the data sets followed by a general description of the hydrographic conditions on the shelf. Next, we examine characteristics of the bottom and surface mixed layers. Using a simple set of models, we investigate the ability of the atmospheric forcing to overturn the water column within small leads, creating a single layer. Lastly, we discuss implications of this convective overturning for primary production on the shelf. The results of our study provide valuable insights into the functioning of the ecosystem on the Chukchi shelf, particularly because the formation, timing, and distribution of high-nutrient winter water are intimately connected to the development of phytoplankton blooms.

2. Data and Methods

In response to the discovery of massive under-ice blooms in the Chukchi Sea (Arrigo et al., 2012), a field program was carried out in late spring 2014 entitled "The Study of Under-ice Blooms In the Chukchi Ecosystem" (SUBICE). This consisted of an interdisciplinary cruise with measurements of the physical, chemical, and biological state of the water column, sea ice, and benthos. The main goal of the SUBICE cruise was to sample pre-, during, and post-bloom conditions as a means to understand how and why these blooms occur and the

physical drivers behind them. The present study focuses on the physical measurements collected during the field program.

2.1. Shipboard Hydrographic and Velocity Data

The shipboard hydrographic and velocity data used in the study were obtained during a 6-week cruise on the USCGC *Healy*, 16 May to 20 June 2014. During this time, 251 water column stations were occupied comprising 15 transects (Figure 2). Due to difficult ice conditions, we were unable to sample the northeasternmost portion of the shelf, including Barrow Canyon. Also, in this study, we do not consider any of the data south of Cape Lisburne. At each station, a Sea-Bird 911+ conductivity-temperature-depth (CTD) system was mounted on a 12-position rosette with 30-L bottles. The temperature sensors were calibrated at Sea-Bird before and after the cruise, and the accuracy was determined to be 0.001°C. Because the Chukchi shelf is so shallow, the bottle salinity samples were not effective for calibrating the conductivity sensors. As such, following previous studies (Pickart et al., 2010; Pisareva et al., 2015), we regressed the conductivity data from the two sensors against each other, which showed a tight relationship (after removing outliers). Based on this, the accuracy of the salinity measurements was deemed to be 0.008. Nutrients were measured from the water samples, typically at the following depths: 2, 5, 10, 25, 50, 75, and 100 m, including a sample at the fluorescence maximum and one just above the bottom. The nutrient analyses were done using a Seal Analytical continuous flow Auto-Analyzer 3, following a modification of the method used by Armstrong et al. (1967).

Velocity of the water column was measured using *Healy's* vessel-mounted RDI Ocean Surveyor 150 kHz acoustic Doppler current profiler (ADCP). The vertical coverage of the ADCP extends from approximately 18 m below the surface to approximately 10–15 m above the seafloor. Due to the extensive ice cover encountered during most of the cruise, velocity profiles were only obtained at the station sites (i.e., while the ship was not steaming). The reader is referred to Pickart et al. (2016) for a description of the processing procedure, including calibration and the use of bottom tracking. After the velocities were calculated, the barotropic tidal signal was removed from each profile using the Oregon State University model http://volkov.oce.orst.edu/tides (Padman & Erofeeva, 2004).

As part of the analysis, vertical sections of hydrographic variables were constructed. This was done using a Laplacian-spline interpolation scheme with a typical grid spacing of 5 km in the horizontal and 2 m in the vertical for the CTD variables, and 10 km and 10 m, respectively, for nutrients. The variables considered are potential temperature referenced to the sea surface (hereafter referred to simply as temperature), salinity, potential density referenced to the sea surface (hereafter referred to as density), and nitrate. In addition, sections of absolute geostrophic velocity were made by referencing the thermal wind shear to the direct ADCP measurements following the procedure in Pickart et al. (2016).

Most of the CTD profiles on the shelf had a two-layer structure: a surface mixed layer separated from a bottom boundary layer by a sharp interface. A typical station is shown in Figure 3 (from the central part of the shelf). Using a MATLAB graphical user interface, we determined various characteristics of the surface and bottom mixed layers. The vertical extent of each layer was determined following the technique used by Pickart et al. (2002). Specifically, each layer was initially identified visually using the graphical user interface, then a two standard deviation envelope was plotted over these two regions (red lines in Figure 3). The final mixed layer depths were then taken to be the locations where the profile passed permanently outside of the envelopes. In the example shown in Figure 3, the surface mixed layer is slightly stratified in temperature, but is neutrally stable in both salinity and density. The bottom boundary layer displays a small degree of stratification, but this is within the precision of the conductivity sensor. For each mixed layer, we determined a line of best fit (blue lines in Figure 3). We also tabulated the change in density between the surface and bottom mixed layers, which hereafter is referred to as the density jump.

2.2. Meteorological Data

Wind measurements were obtained on the *Healy* using four sensors: one acoustic anemometer on the bow mast, one on the starboard yard arm, and mechanical anemometers on the starboard and port yard arms (the yard arm is a horizontal pipe located above the ice pilot station). A comparison of these records indicated that each of the sensors had problems during portions of the cruise, likely caused by blockage from the ship's superstructure. It was deemed that the bow mast unit was the least reliable, so we constructed a timeseries

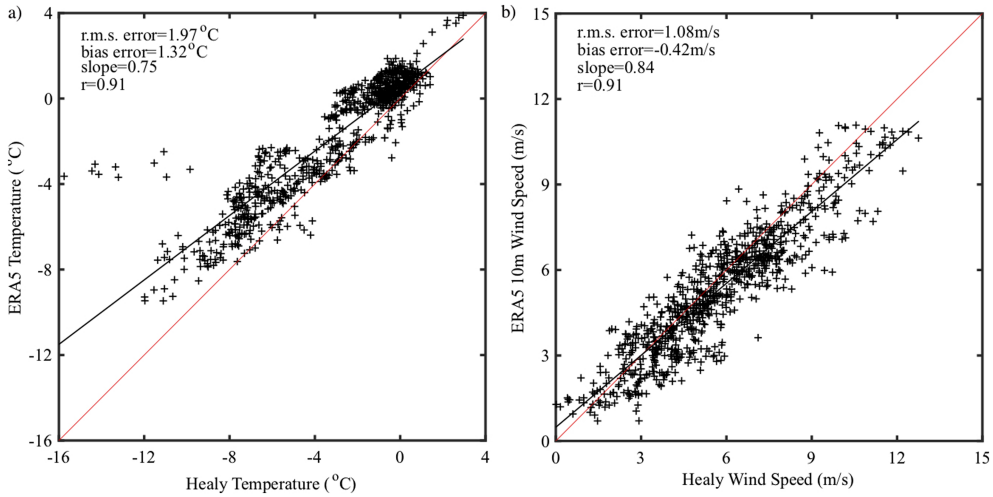

Figure 4. Scatterplots of the observed versus interpolated ERA5 data for the (a) surface air temperature (°C) and (b) surface wind speed (m/s) along the 2014 *Healy* ship track. The black lines are the best fits, and the red lines are the one-to-one fits.

based on the yard arm sensors only, selecting the side with least blockage as indicated by the relative wind direction. When available, we used the data from the mechanical sensors since the acoustic yard arm sensors showed occasional drops in absolute wind speed, even when blockage was minimal. Shipboard air temperature was collected by three RM Young temperature probes (model 41342), one of them part of a relative humidity sensor (HRH, model 41382), located on *Healy's* Jack Staff and above the bridge. Since the Jack Staff unit failed, we used the data from the bridge sensor located 23 m above the water line. This record displayed generally good agreement with the nearby HRH unit. The sensors were calibrated in February of 2014, and we estimate the instrument accuracy to be within 0.1 °C (Carl Mattson, pers. comm., 2019). Data are available from http://ocean.stanford.edu/subice/.

For the part of the analysis involving air-sea buoyancy forcing, we use the ECMWF Integrated Forecast System (IFS) ERA5 reanalysis product (Hersbach & Dee, 2016). The spatial and temporal resolution is 0.25° and 1 hr, respectively. We use data for March, April, May, and June 2014. In addition to bulk fields such as the 2-m air temperature and the 10-m wind speed, the fluxes of sensible and latent heat across the air-sea interface as well as the net surface long and shortwave radiative fluxes were also used. To compare the reanalysis and in situ data, we extracted the ERA5 information at the closest grid point in space and time following the track of the ship.

The scatterplot of observed versus analyzed 2 m air temperature and 10 m wind speed show a high degree of correlation, $r \sim 0.9$, for both cases (Figure 4). With respect to the 2-m air temperature, the rms error was ~2 °C, with a warm bias of ~1.3 °C. For the 10-m wind speed, the rms error was ~1 m/s with the ERA5 underestimating the measured wind speeds by ~0.4 m/s. There were no in situ measurements of the surface fluxes available for this cruise. Previous work has indicated that the IFS model used in the ERA5 reanalysis is able to accurately capture and represent the variability in the high-latitude air-sea heat fluxes (Petersen & Renfrew, 2009; Renfrew et al., 2002). Information on the ability of the IFS model to represent the surface net radiative fluxes is less certain, mostly due to issues with the representation of cloud processes (Chauduri et al., 2014; Walsh et al., 2009). However, among a broad set of atmospheric reanalyses, those based on the IFS model tend to have low biases in both long and short wave fluxes (Chauduri et al., 2014; Lindsay et al., 2014; Walsh et al., 2009).

2.3. Satellite Ice Data

Our study uses Advanced Microwave Scanning Radiometer 2 (AMSR-2) data to characterize the sea ice concentration on the shelf over the winter and spring of 2014. AMSR-2 is a 6.25-km product with daily resolution. The data come from the Global Change Observation Mission 1st-Water satellite. It measures seven frequency bands from 6.925 to 89.0 GHz (Beitsch et al., 2014). The data were downloaded from the University of Bremen (http://www.iup.uni-bremen.de:8084/amsr2data/asi_daygrid_swath/n6250/2014/).

2.4. Polynya Model

As part of our analysis, we use a polynya model to estimate the production of salt due to the formation of ice. The model is the same as that employed by Pickart et al. (2016). It is used here both in a stationary frame of reference and in a Lagrangian frame, following parcels being advected northwards through the Chukchi Sea. The model calculates sea ice production according to

$$P = \frac{Q_{\text{net}}}{\rho_{\text{ice}} L_{\text{h}}},$$

where Q_{net} represents the net cooling surface flux (W/m^2), ρ_{ice} represents the density of sea ice (kg/m^3), L_{h} represents the latent heat of fusion (J/kg; Cavalieri & Martin, 1994), and P represents the rate at which ice is produced (kg/s).

The salinity of the new ice, S_{i}, is

$$S_{\text{i}} = 0.31 S_{\text{w}},$$

where S_{w} represents the salinity of the surface water. The model combines these two equations to obtain the salt flux according to

$$F_{\text{s}} = \rho_{\text{ice}}(S_{\text{w}} - S_{\text{i}}),$$

where F_{s} represents the salt flux generated by sea ice formation (Cavalieri & Martin, 1994).

In the stationary reference case (section 3.2.2), the salt flux is calculated at a time step of 10 min. This is subsequently used as input to a one-dimensional mixed-layer model (see below) to investigate convective overturning of the water column. In the Lagrangian case (section 3.2.3), the salt flux is calculated daily, following water parcels with the assumption that the surface water is at the freezing point. Polynya conditions are assumed to prevail when the ice concentration is less than 80%. The salt produced is assumed to mix throughout the water column, and the resulting change in salinity following the parcel is tabulated. The reader is referred to Pickart et al. (2016) for details of the Lagrangian application of the model.

2.5. One-Dimensional Mixing Model

To investigate the ability of the water column to overturn due to brine rejection during ice formation, we employ the one-dimensional mixing model of Price et al. (1986), hereafter referred to as the PWP model. The model is initialized using CTD profiles from the cruise under open water conditions. Initially, the heat flux cools the water, and once the sea surface temperature reaches the freezing point, the model is driven solely by the negative freshwater flux calculated using the polynya model described above. The momentum is assumed to be zero throughout. The vertical resolution used for the PWP model is 1 m, and we run it with a time step of 10 min. All of the initial CTD profiles have a surface mixed layer, and the model is used to document the deepening of the layer due to the negative freshwater flux from the surface. The model computes the evolution of the stratification by computing the gradient Richardson number, the bulk Richardson number, and the vertical density gradient (Price et al., 1986). The MATLAB code for this model can be found at https://www.mathworks.com/matlabcentral/fileexchange/68807-pwp.

3. Results and Discussion

3.1. Hydrographic Setting

3.1.1. Water Mass Distribution

A variety of water masses are found on the Chukchi shelf throughout the course of a year. The cold winter water (near the freezing point) that flows northward through Bering Strait from approximately January through April (Woodgate et al., 2005) is referred to as newly ventilated winter water (NVWW). As this water warms later in the season, either via solar heating or mixing with summer water masses on the shelf, it becomes remnant winter water (RWW). RWW constitutes the cold halocline layer in the Canada Basin (e.g., Steele et al., 2004). In addition to these two winter water masses, there are two types of Pacific-origin summer waters that are found seasonally on the Chukchi shelf. Chukchi summer water (CSW) is a combination of Anadyr water and central Bering shelf water that mix with each other north of Bering Strait on the

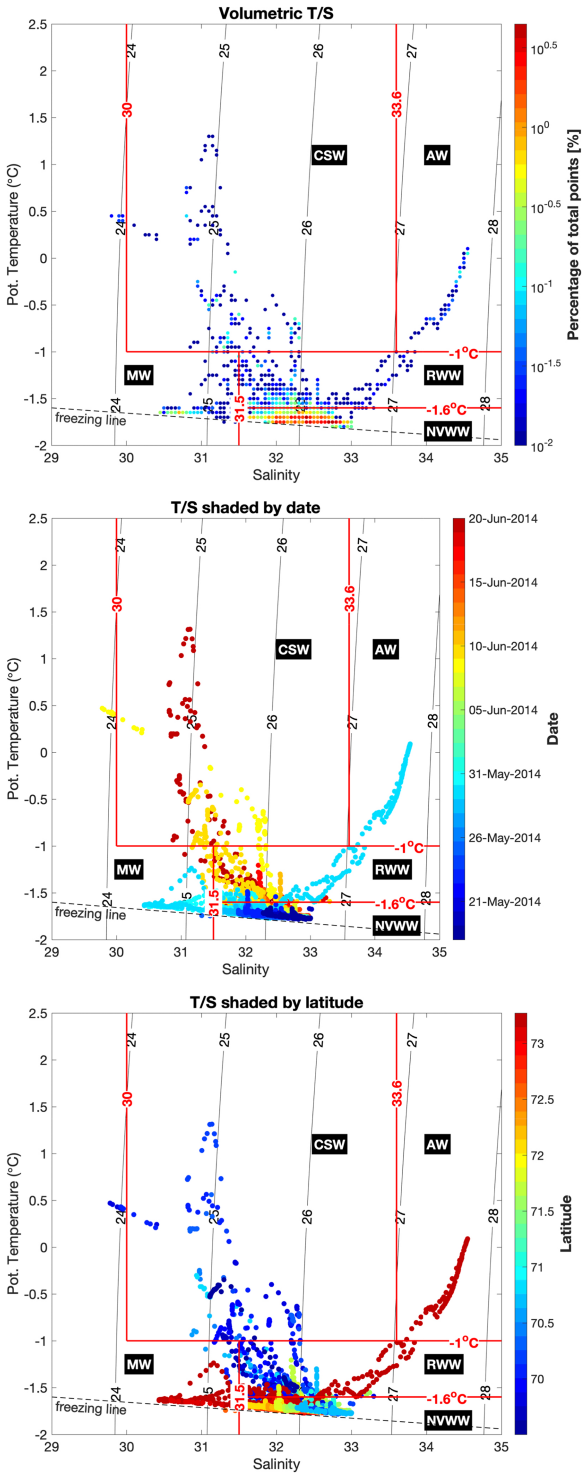

Figure 5. (a) Volumetric T/S diagram for all the stations occupied north of 68°N during the cruise. The color denotes the number of points within bins of 0.05°C in temperature by 0.05 in salinity. The water mass boundaries are denoted by the red lines. The freezing line is indicated. The water masses are: NVWW = newly ventilated winter water; RWW = remnant winter water; CSW = Chukchi summer water; MW = meltwater; and AW = Atlantic water. (b) The same T/S diagram except that the points have been colored by date of occupation. (c) Same as (b) except the points have been colored by latitude.

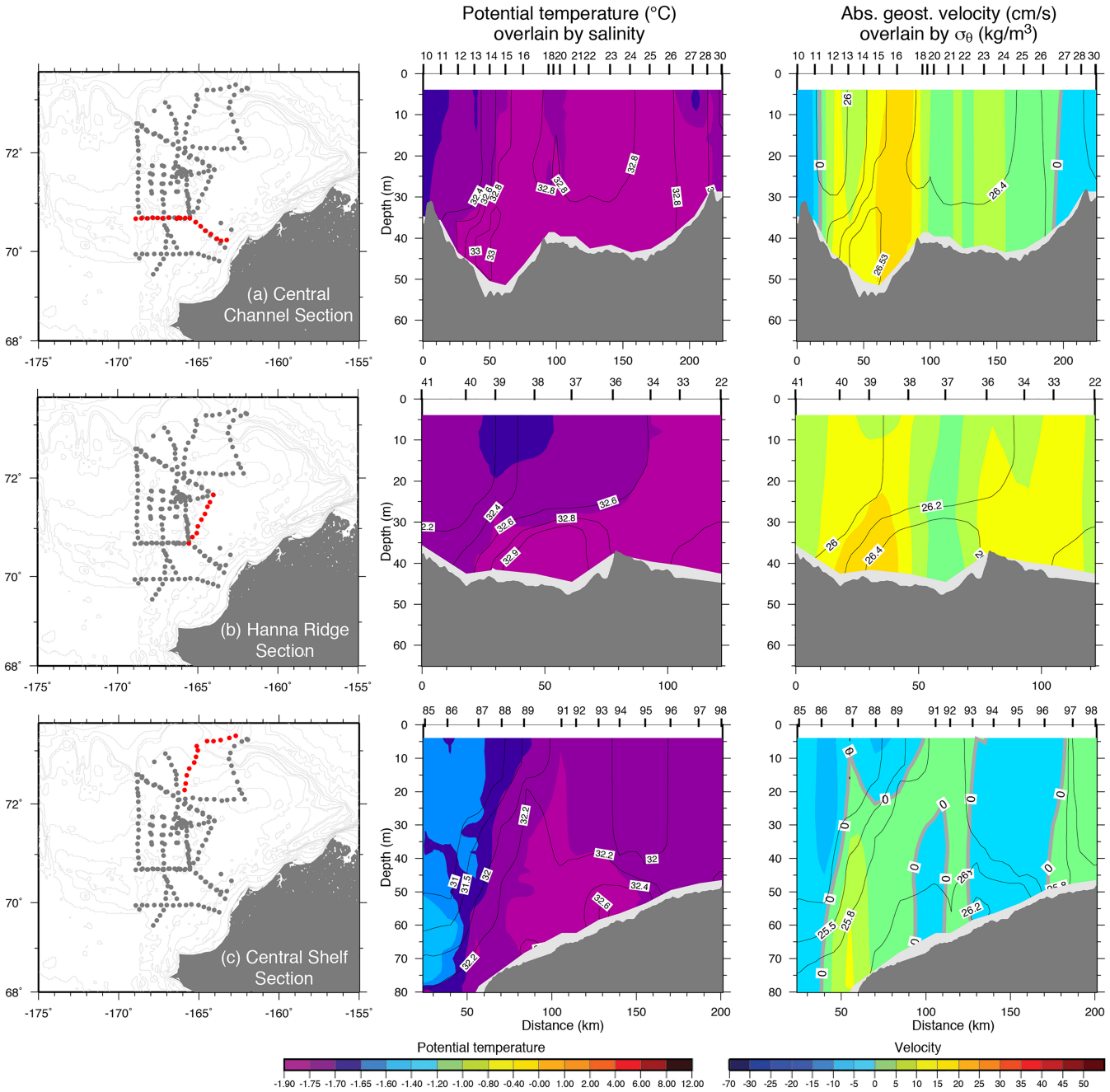

Figure 6. Vertical sections of potential temperature (color) overlain by salinity (contours), and absolute geostrophic velocity (color) overlain by potential density (contours). Positive velocities are into the page, flowing northward/eastward. The bathymetry is from the ship's echo sounder. Station numbers are listed along the top. (a) The Central Channel section (station 10—westernmost station); (b) the Hanna Ridge section (station 41—northernmost station); (c) the central shelf section (station 85—northernmost station). The left-hand panel in each row shows the location of the transect (red-colored stations).

southern portion of the shelf (e.g., Gong & Pickart, 2015, 2016; von Appen & Pickart, 2012). This water mass has also been referred to as western Chukchi summer water (Shimada et al., 2001), summer Bering Sea water (Steele et al., 2004), and Bering Summer Water (Pisareva et al., 2015). The second Pacific-origin summer water is the Alaskan coastal water (ACW), which is warmer, fresher, and more strongly stratified than CSW. It enters the Chukchi Sea via the Alaskan Coastal Current.

The final three water masses found in the Chukchi Sea are sea-ice meltwater (MW), Siberian coastal water (SCW), and, on occasion, Atlantic water (AW). The former has two varieties (e.g., Gong & Pickart, 2015): early-season MW, which is near the freezing point, and late season MW, which has been warmed by solar heating. AW is transported eastward along the continental slope of the Chukchi Sea by the Arctic-wide cyclonic boundary current system (Aagaard, 1984; Aksenov et al., 2011; Karcher et al., 2007; Rudels et al., 2004). Periodically, this warm and salty water is upwelled into Barrow Canyon in the east (e.g. Aagaard & Roach, 1990; Pisareva et al., 2019) and Herald Canyon in the west (Pickart et al., 2010). Under certain circumstances, the AW can penetrate far onto the shelf (Bourke & Paquette, 1976; Ladd et al., 2016). The SCW originates as runoff from the Siberian coast and is found predominantly in the Siberian Coastal Current, which flows towards Bering Strait (e.g., Weingartner et al., 1999). At times, this water mass can be found in Herald Canyon and also on the central shelf (Pisareva et al., 2015).

A typical summertime survey of the Chukchi Sea will measure many (if not all) of these water masses (e.g., Gong & Pickart, 2015; Pisareva et al., 2015). During our late spring survey, however, the majority of the water on the northeast Chukchi shelf was NVWW (Figure 5a). Here, we define NVWW as colder than −1.6 °C and saltier than 31.5, a definition consistent with past studies (e.g., Gong & Pickart, 2015; Itoh et al., 2015; Pickart et al., 2016). As noted in section 1, NVWW can be further transformed within the northeast Chukchi polynya to form a very salty water mass known as hypersaline winter water. Weingartner et al. (1998) defined two classes of this salty water—one with salinities between 33 and 33.6 and the other with salinities >34. As seen in Figure 5a, neither of these hypersaline classes were observed during the SUBICE cruise (keep in mind that we were unable to sample the very northeast part of the shelf; Figure 2). Excluding the stations seaward of the shelfbreak (and the Bering Strait transect occupied at the start of the cruise), more than 96% of the water measured during the cruise was NVWW, as computed from a temperature-salinity (T/S) census, where all T/S values are computed (for each bin of CTD data) and those within NVWW T/S space are tallied (Figure 5a).

To shed light on the space/time patterns of the different water masses sampled on the cruise, we constructed T/S plots based on time (Figure 5b) and latitude (Figure 5c). Clear patterns emerged. The coldest NVWW (i.e., near the freezing point) was sampled early in the cruise (in late May, Figure 5b). Not surprisingly, most of the RWW was measured in June, that is, after the coldest winter water started to moderate. Nearly all of the CSW was measured at the end of the cruise, at which time the leading front of the Pacific-origin summer water was entering the domain. There is also a clear division between the early-season MW and late-season MW. Geographically, all of the AW was located at the northern end of the domain, in particular, seaward of the shelfbreak (Figure 5c). This is also where we sampled the early-season MW, providing evidence of sea ice melt off of the shelf. The late-season MW was observed in the southern part of the domain in the vicinity of the retreating ice edge (see also Figure 2). Consistent with the timing noted above, the CSW was confined to the southern end of the study region. Similarly, most of the RWW was found in this region as well. Finally, note that the NVWW was observed throughout the range of latitudes sampled on the cruise.

3.1.2. Water Column Structure

Vertical sections were constructed for each of the 15 transects occupied during the cruise. Here, we show three of the transects in order to point out some of the features that were unique to this late-spring survey (Figure 6). The first section extends across the Central Channel towards the Alaska coast (referred to as the CC line in Figure 2). This was the first transect sampled on the Chukchi shelf (north of Bering Strait) from 18 to 20 May. Strikingly, the entire section consisted of NVWW. Previous early-summer hydrographic surveys showed that this cold water mass was confined to the major flow pathways (Pickart et al., 2016). Clearly, this is not the case earlier in the season. The saltiest winter water was found in the Central Channel (Figure 6a), but the coldest winter water was found on the eastern portion of the transect. (Note: this is not evident from the temperature color bar in Figure 6; we have chosen this color bar to be consistent with numerous previous studies.) The section of absolute geostrophic velocity reveals the Central Channel flow branch, which exceeds 15 cm/s on the eastern side of the channel. While there is NVWW everywhere in the section, the saltiest (and therefore densest) winter water is confined to the major flow path passing through the channel.

The next transect we consider is the Hanna Ridge line (section HR in Figure 2), which was occupied 22–23 May (shortly after the CC section). This was positioned along a portion of the corrugated ridge between Herald and Hanna shoals (the biggest gap in the ridge is of course the Central Channel; see the

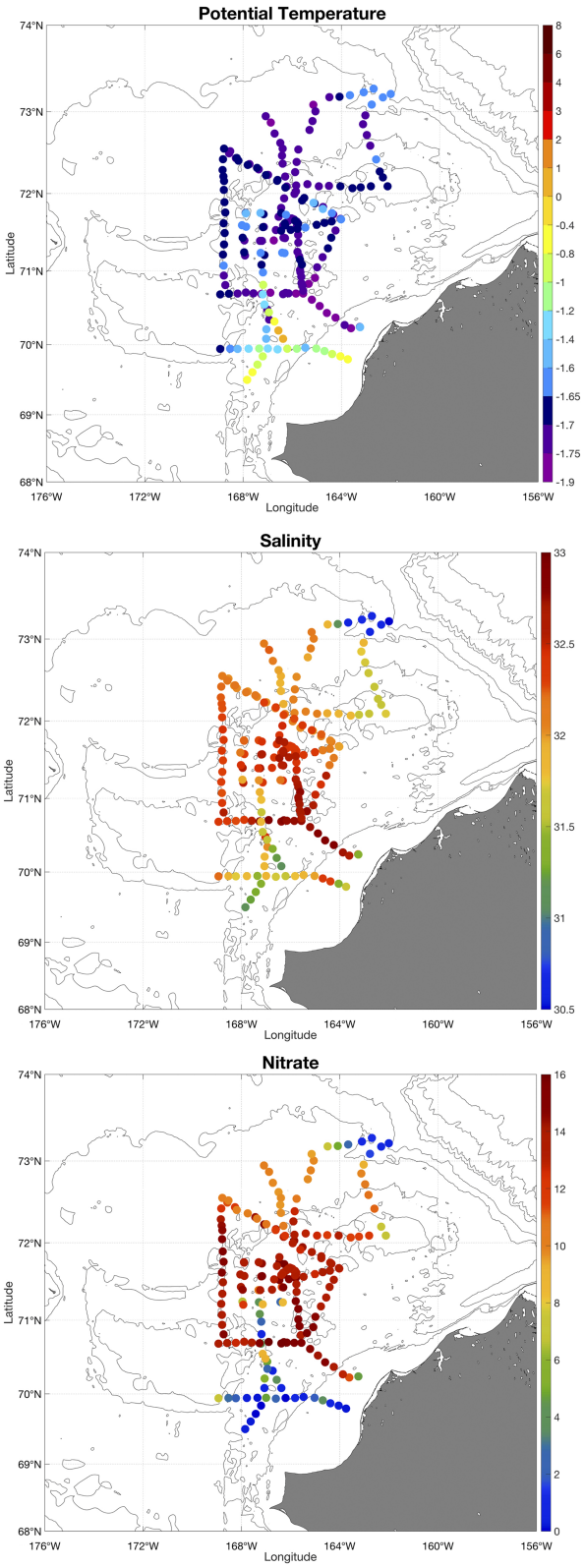

Figure 7. Lateral property plots. (a) Potential temperature (°C) averaged over the top 25 m of the water column. The bathymetry is from IBCAO version 3; (b) same as (a) except for salinity; (c) same as (a) except for nitrate (μM/L).

bathymetry in Figure 2). As with the CC line, this section contained exclusively NVWW (Figure 6b). The notable aspect of this transect is that the small bathymetric depression (between stations 36 and 40) contains the saltiest and densest water. Furthermore, the northern side of this dense feature is associated with a bottom-intensified geostrophic current to the east. Together with nearby data (see section 3.1.5 below), this implies that NVWW is "leaking" from the main Central Channel flow pathway to the east through gaps in the ridge. As was the case with the CC section, the saltiest winter water is embedded within a region of enhanced flow, suggesting that while NVWW is prevalent everywhere, the currents on the shelf advect the densest variety of this water mass.

The final section we present is the CEN line, which extends from the upper continental slope to the outer portion of the shelf (Figure 2). This was one of the two sections that crossed the shelfbreak, and it reveals that the NVWW was confined to the Chukchi shelf. Seaward of the shelfbreak, the dominant water mass in the basin was RWW (seen in the light blue shading in Figure 6c, middle panel), which was clearly more than a year old (i.e., ventilated on the Chukchi shelf during a previous winter). This water appears in the T/S plots shown above as the only RWW that was sampled both early in the cruise (Figure 5b) and at the northern latitude (Figure 5c). On the shelf, there is nothing but NVWW, some of it very weakly stratified (station 96 had a neutrally stable density profile from top to bottom). The density front at the edge of the shelf between the NVWW and RWW supports a bottom-intensified, eastward-flowing shelfbreak jet, which has been observed previously (e.g., Corlett & Pickart, 2017; Li et al., 2019; Mathis et al., 2007; Pickart et al., 2016).

3.1.3. Lateral Patterns

The volumetric T/S diagram (Figure 5a), together with the vertical sections, indicate that most of the domain sampled during the SUBICE cruise contained NVWW. To assess if there were any spatial patterns, we constructed lateral maps. As mentioned above, a previous early-summer survey in 2011 measured NVWW only within the main flow pathways and it was mainly restricted to the lower part of the water column. To highlight the difference in the hydrographic nature of the shelf during the late-spring time period, we averaged the properties at each of the stations in the upper 25 m of the water column (which for the previous surveys would show very little, if any, winter water). The resulting distribution of average temperature reveals that NVWW occupied the surface layer over most of the measurement domain (Figure 7a). The main exceptions were the region seaward of the shelfbreak and the southern portion of the study area, which was sampled at the end of the cruise. Much of the region south of the CC line was in open water at that point, and the warm temperatures are indicative of RWW (with some CSW and late-season MW near the surface). Recall that NVWW is defined as water colder than −1.6 °C. Hence, there was spatial variation in the temperature of this water mass (the coldest NVWW sampled on the cruise was −1.78 °C). While there is no obvious pattern in Figure 6a, the T/S diagrams of Figures 4b and 4c reveal that, early in the cruise, the NVWW was a bit warmer and fresher to the north (progressing along the freezing line).

As was true for the temperature, the salinity values on the continental slope were distinct from the outer shelf; in particular, the basin water was markedly fresher (Figure 7b). Also, in line with the temperature, the water sampled late in the cruise in the southern part of the domain was noticeably different in salinity compared to waters farther north (again fresher, but not as fresh as the basin water). However, in contrast to the temperature, there was a clear lateral trend in the salinity of the NVWW on the shelf. In particular, north of about 72°N, the winter water became fresher by about 0.3. Furthermore, there was a zonal gradient in the salinity of the NVWW, with fresher values closer to Hanna Shoal. This same trend in NVWW salinity was found by Pickart et al. (2016) using early summertime data, except in that case the average was done for the deep part of the water column (where the NVWW was found). We investigate this lateral salinity trend further in section 3.2.3.

As noted in section 1, the NVWW is critically important to the regional ecosystem because of its high nutrient content, which spurs primary production (Hill & Cota, 2005; Lowry et al., 2015, 2018; Pickart et al., 2016). Our SUBICE cruise revealed that in late spring, the nitrate levels in the upper part of the water column are generally quite high (see also Arrigo et al., 2017). Figure 7c shows the average value over the top 25 m (the distribution is nearly identical if only the near-surface values are plotted). The water seaward of the shelf is low in nitrate since, as noted above, it is MW. In the southern part of the domain, the levels are low because the nitrate has been drawn down due to bloom activity in the nearly open water encountered late in the cruise. Another region of low nitrate was found on the eastern end of the CC line (near Icy Cape). As seen in Figure 6a, this region contained NVWW, yet the nitrate concentration in the upper 25 m was fairly low.

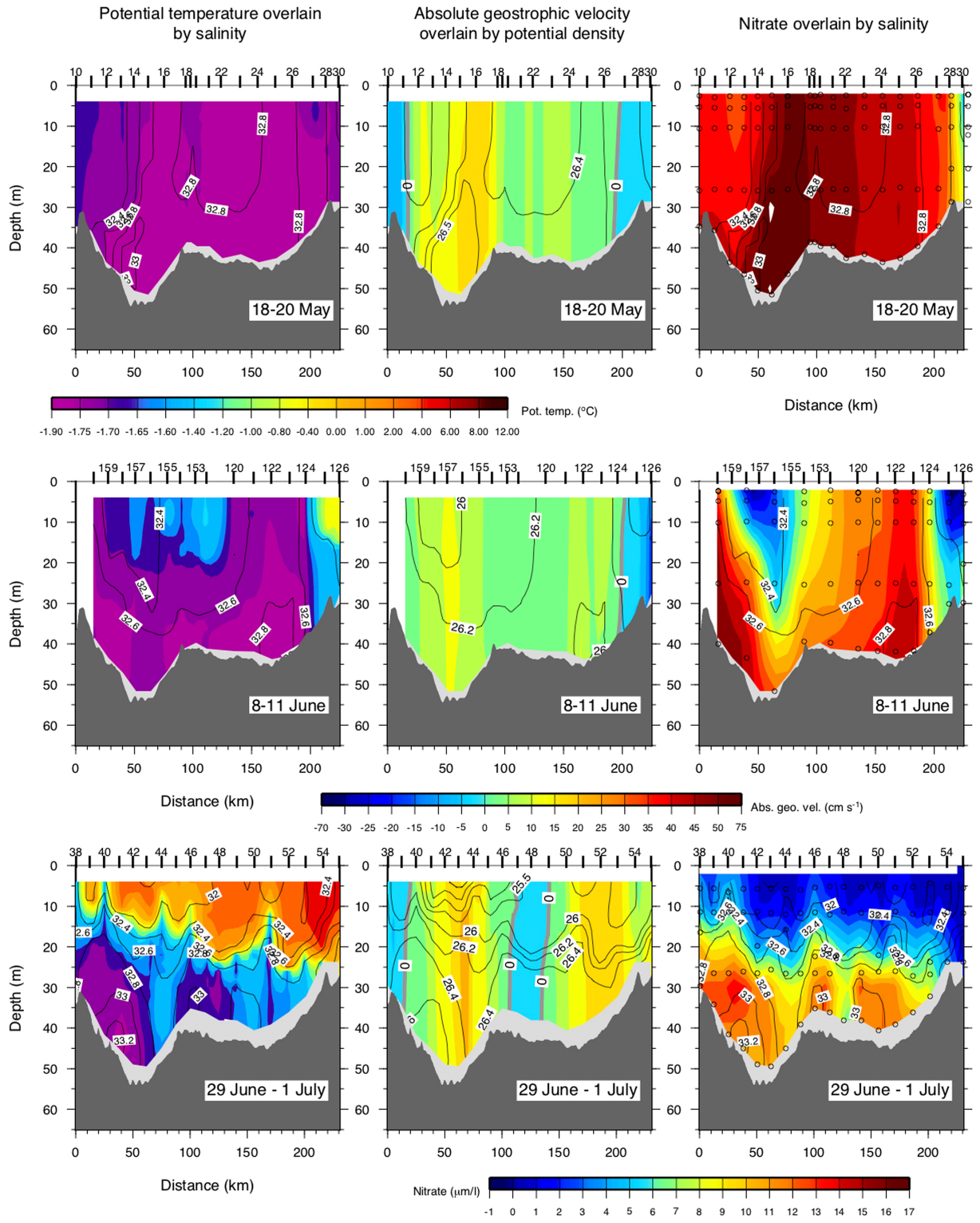

Figure 8. Repeat occupations of the Central Channel section (section CC in Figure 2). Top row: 18–20 May, 2014; middle row: 8–11 June, 2014; bottom row: 29 June to 1 July, 2010. The left-hand column shows sections of potential temperature (color, °C) overlain by salinity (contours). The middle column shows sections of absolute geostrophic velocity (color, cm/s) overlain by potential density (contours, kg/m^3). The right-hand column shows sections of nitrate (color, μM/L) overlain by salinity (contours), where the circles denote the water sample locations. Station numbers are listed along the top of each plot.

During the occupation of the eastern portion of this line, the winds were northerly and the flow near the coast was to the south. This suggests that anomalous nutrient conditions coincided with the anomalous flow direction.

In the central portion of our study domain—where the NVWW was located—the lateral distribution of nitrate shows a similar pattern to that of the salinity (compare Figures 7b and 7c). In particular, the nitrate concentrations in the upper water column are significantly lower north of 72°N. Regressing nitrate against salinity (excluding the continental slope stations and the sections occupied at the end of the cruise) reveals a statistically significant relationship, with saltier NVWW generally higher in nitrate (see also Arrigo et al., 2017). The likely reasons for this are explored in section 3.2.3.

3.1.4. Temporal Evolution

During the cruise, we occupied the CC section (across the Central Channel, Figure 2) in mid-May (early in the cruise) and again in early June. In addition, the section was occupied in late June in 2010 during a previous field program (Pickart et al., 2016). This provides the opportunity to look at the evolution of the water column at this location during the spring to summer transition. We consider the hydrography, velocity, and nitrate concentration (Figure 8). The first occupation was discussed previously, but in Figure 8 (top row), it is now evident that the saltiest NVWW in the Central Channel pathway was also the highest in nitrate. We hasten to add, however, that the nitrate concentrations were high throughout the section with very little vertical structure. The only exception was near the coast in the reversed flow.

Three weeks later, the conditions had changed considerably (Figure 8, middle row). Warmer, fresher water (but still within the T/S range of NVWW) was present in the upper 20 m of the water column in the Central Channel, presumably advected there via the middle flow pathway (see Figure 1). This pathway is again evident in the section of absolute geostrophic velocity. One sees that the nitrate in this region is largely drawn down, which likely took place upstream in near-open water (the ice cover over the Central Channel during the second occupation was still >90%). Low nutrient concentrations were also found at the eastern end of the section in the region of reversed flow, as was the case in the earlier occupation. Unlike the first transect, however, the (much lower) nutrient values in early June near the coast were likely due to local draw down. This is consistent with the reduced ice cover there (30% versus 100% during the first crossing in mid-May), which also can explain the presence of RWW and CSW near the coast due to local solar heating. The last feature of note in the second occupation is the high nutrient signal at stations 122–123. This is associated with salty NVWW embedded within a region of enhanced northward flow. Hence, while the Central Channel pathway was advecting dense nitrate-enriched winter water northward in the first crossing, the same was true of the coastal pathway in the second crossing.

The transect in late June (occupied in 2010) showed a vastly different situation. The upper half of the water column was filled with warm CSW, separated by a halocline from winter water near the bottom (Figure 8, bottom row). There were three "pockets" of NVWW: one in the Central Channel pathway, one in the coastal pathway, and one within a region of weak southward flow between the two pathways. As discussed in Pickart et al. (2016), these were the last vestiges of NVWW flowing through the Chukchi Sea. Each of the three regions of NVWW was associated with enhanced nitrate, while the nitrate levels in the CSW were generally low due to drawdown by open water blooms locally on the Chukchi shelf. The highest levels of chlorophyll were found at the interface between the NVWW and CSW (not shown), emphasizing the importance of the NVWW in driving primary production, even at depth (see Lowry et al., 2015 for details).

3.1.5. Velocity Field

In the repeat occupations of the CC transect presented in the previous section, one sees that both the Central Channel pathway and the coastal pathway were present in each of the three realizations (the flow was strongest in the 2010 occupation). Using data primarily from an early summer survey of the Chukchi Sea in 2011, Pickart et al. (2016) constructed a circulation scheme for the northeast Chukchi shelf, which is depicted schematically in Figure 1. Since that study, the circulation along the Chukchi shelfbreak and slope has been revised (see Corlett & Pickart, 2017; Li et al., 2019), which is reflected in Figure 1. The new features presented in Pickart et al. (2016) were: (1) the flow bifurcates west of Hanna Shoal then progresses around each side of the shoal; (2) a portion of the western flow branch diverts eastward on the north side of Herald Shoal and joins the central branch; and (3) some of the flow from the central branch "leaks" through the corrugated ridge between Herald and Hanna Shoals and progresses towards Barrow Canyon. It is of interest to know if our SUBICE survey indicates similar features.

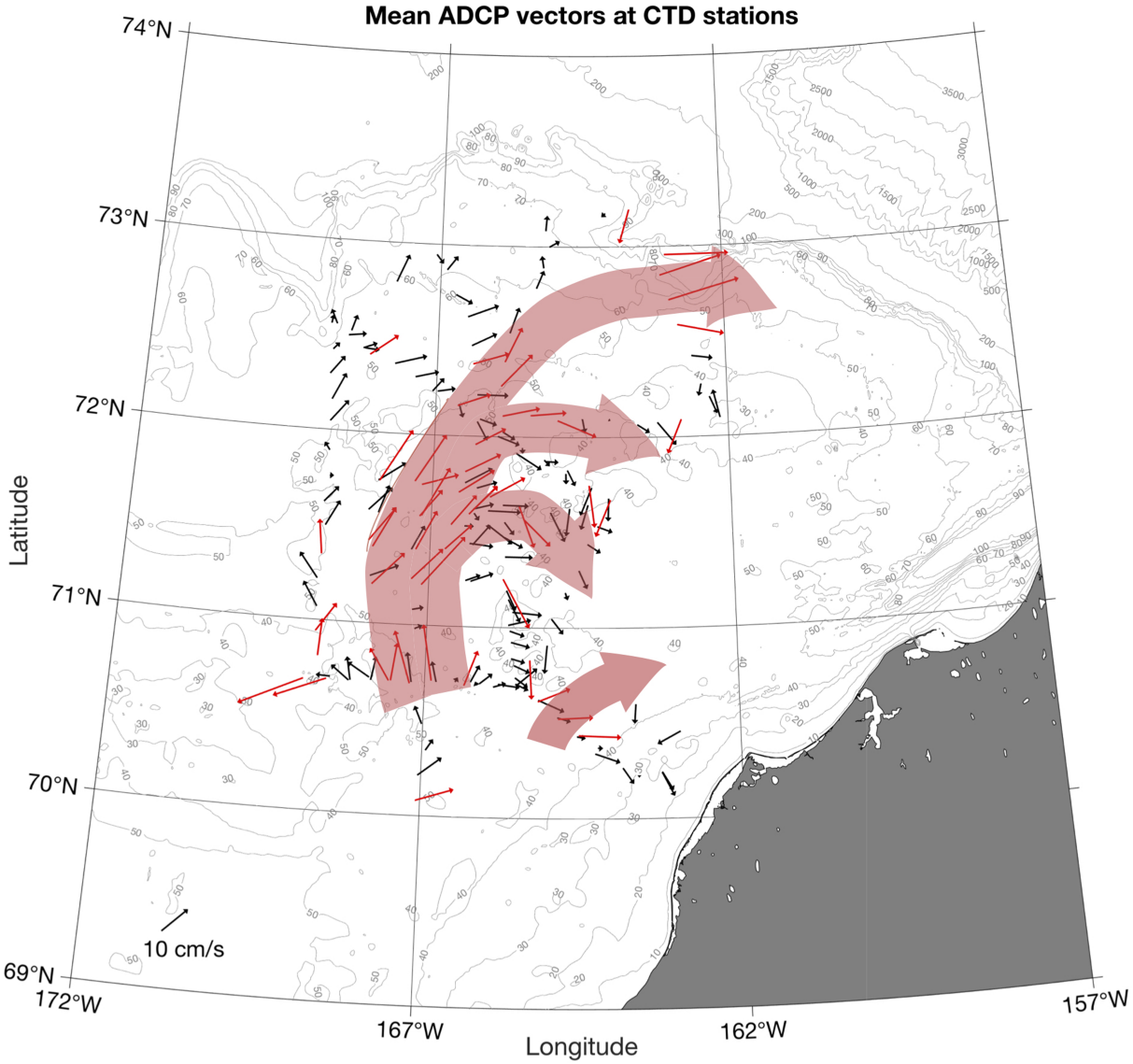

Figure 9. Depth-averaged velocity vectors from the shipboard acoustic Doppler current profiler. The vectors with magnitude >10 cm/s are colored red. The transparent red arrows are meant as a guide to show the main flow pathways on the shelf.

In Figure 9, we present the depth-averaged ADCP flow vectors from our survey. The vectors that exceed 10 cm/s are colored red, which reveals the major flow paths (the red-shaded arrows are simply meant as a guide to the reader). Overall, the flow field measured in late spring 2014 was remarkably consistent with that measured in early summer 2011. In particular, the Central Channel pathway is evident, and one sees that the flow divides around the northern and southern sides of Hanna Shoal. There is also a signature of the coastal pathway (see also the vertical sections of absolute geostrophic velocity in Figure 8). Interestingly, one gets the impression that the coastal pathway bifurcates from the Central Channel pathway between 70–70.5°N. This is entirely feasible since at this time of year, the coastal pathway is not the Alaskan Coastal Current (which develops later in the season).

Outside of the main pathways, the flow field in Figure 9 is also in line with the circulation scheme in Pickart et al. (2016). Clearly, a significant amount of flow progresses eastward through the corrugated ridge between Herald and Hanna Shoals. One example of this was shown above for the HR section (Figure 6b), but it seems to happen all along the ridge to varying degrees. A second example is the slightly tighter recirculation limb centered at 71.5°N. This southeastward migration of waters has been previously observed and thus appears

to be a persistent feature (Pickart et al., 2016; Lin et al., 2019). The notion that part of the western pathway joins the central pathway is also supported by the SUBICE measurements (note the flow to the northeast between 72 and 72.5°N in the northwest part of the study domain). Finally, the flow along the upper continental slope is an expression of the Chukchi shelfbreak jet. The consistency of the flow field presented here with that of Pickart et al. (2016) suggests that these various features are permanent aspects of the circulation of Pacific-origin water on the Chukchi shelf—at least in spring and summer.

3.2. Mixed Layers

As discussed above, the majority of the CTD profiles occupied during the survey displayed a two-layer structure, with a surface mixed layer and bottom boundary layer separated by a sharp density interface (see Figure 3 for a typical example). Out of the 181 CTD stations occupied on the shelf that contained NVWW, 176 had surface mixed layers, 157 had bottom mixed layers, and 155 had both. Here, we focus primarily on the thickness of the surface and bottom mixed layers and the magnitude of the density jump between them.

3.2.1. Bottom Boundary Layers

There were no obvious geographical or temporal trends in bottom boundary layer height across our survey domain. Previous theory (Lentz & Trowbridge, 1991; Trowbridge & Lentz, 1991) has demonstrated that for flow over a sloping bottom, the thickness of the bottom mixed layer is sensitive to whether the interior flow (i.e., that above the layer, not the wind-driven flow) is upwelling-favorable or downwelling-favorable. In the former case, when the current is flowing with shallow water on the left, the upslope bottom Ekman layer flow tends to advect denser water beneath light water. This enhances the stratification and keeps the bottom layer thin. In the latter case, when the current is flowing with shallow water on the right, the downslope Ekman flow brings light water beneath dense water, which results in a statically unstable condition. The resulting convective adjustment causes the bottom mixed layer to increase in thickness. In the upwelling-favorable scenario, the bottom boundary layers will reach a threshold maximum height, above which they will no longer grow. By contrast, in the downwelling scenario, there is no such impediment on how thick the layer can be.

In an effort to determine if our data are consistent with this theory, we examined the conditions associated with each station and determined if it was an upwelling-favorable case, a downwelling-favorable case, or neither. This entailed considering the ADCP velocity data at the station and the slope of the local bathymetry. In order to get the most accurate estimate of the bottom slope, we used the ship's echosounder data, which was corrected for variations in sound speed and smoothed slightly to remove scatter (we note that the digital databases, such as IBCAO and ETOPO, are not sufficient in terms of resolution or accuracy for this calculation). This bathymetric data meant that we could only consider stations where the ADCP velocity vector was approximately perpendicular to the transect. We also excluded stations that had weak bottom slopes (magnitudes $< 10^{-4}$), which removed a large number of sites from consideration (keep in mind that much of the Chukchi shelf is relatively flat, particularly the region that we sampled). Even after applying these criteria, we detected no systematic differences in the character of the bottom boundary layer heights for the upwelling-favorable versus downwelling-favorable stations. In particular, there were no trends with respect to bottom slope, and the scatter in layer heights was similar in both cases. As shown below, we believe that this was because active convection was taking place prior to and during the first part of the cruise, which would hinder the applicability of the above theory to our observations.

3.2.2. Surface Mixed Layers and Convective Overturning

The average surface mixed layer height over the study domain was 19.8 ± 10.0 m, and there were no distinguishable patterns in space or time. However, one striking aspect of our data set was that the density jump between the surface layer and the bottom layer was typically very small. This in turn suggests that it would not take much surface buoyancy loss, and resulting convective activity, to erode this interface and homogenize the entire water column. In fact, seven stations sampled during the cruise had a density jump of <0.01 kg/m^3. As noted earlier, previous studies using moorings on the Chukchi shelf have documented salinification of the near-bottom water within polynyas (Itoh et al., 2012; Weingartner et al., 1998). The open water quickly freezes and rejects brine into the surface water, which destabilizes the water column. This results in convective overturning, transporting the extra salt to depth. The deep mooring records indicate that the overturning can reach the bottom.

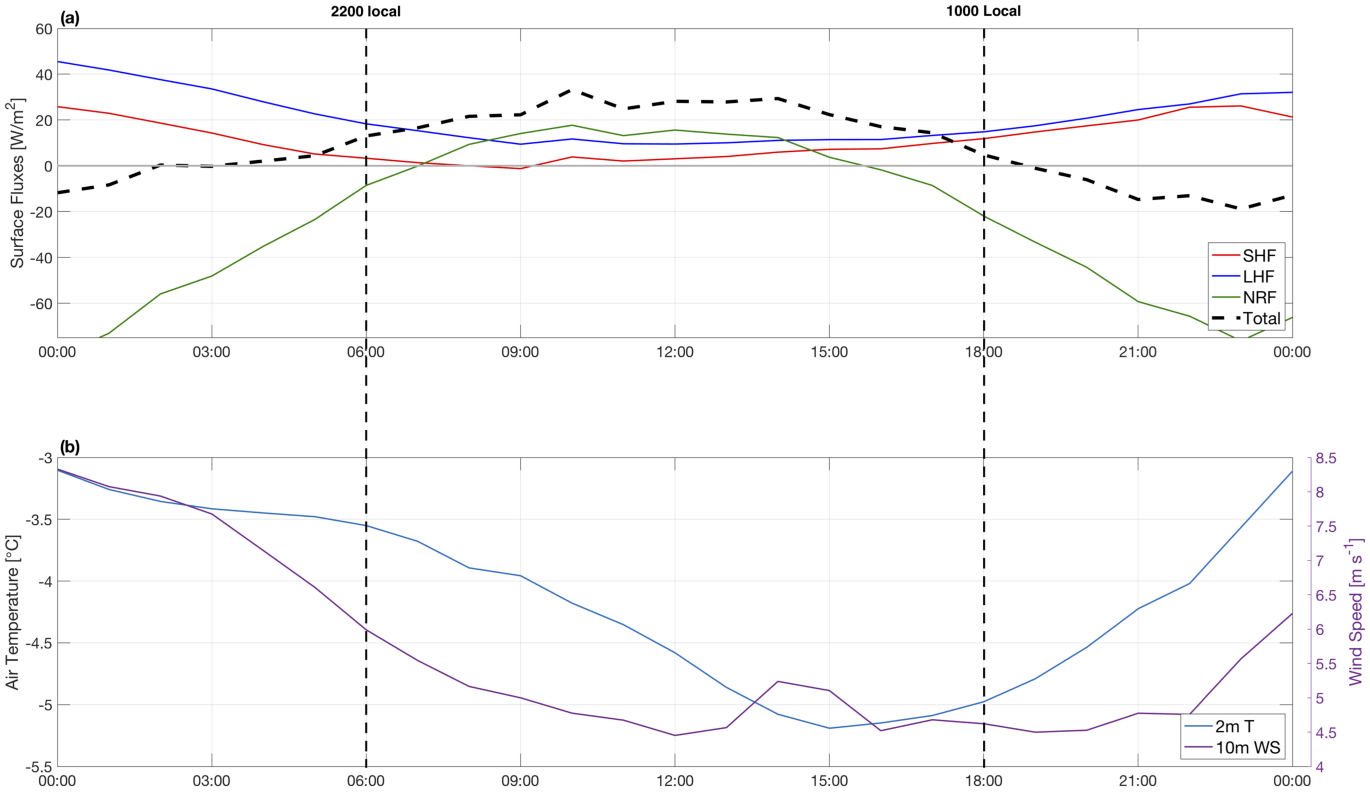

Figure 10. (a) Timeseries of the sensible heat flux (red curve), latent heat flux (blue curve), net radiative flux (green curve), and total heat flux (bold black dashed curve) for a typical diurnal cycle in mid-May, from the ERA5 reanalysis. (b) Timeseries of 10-m wind speed (purple curve) and 2-m air temperature (blue curve) for the same period.

None of the stations in our survey were occupied in the northeast Chukchi polynya, which appears between Point Barrow and Cape Lisburne (e.g., Itoh et al., 2012; Ladd et al., 2016). Also, the satellite data indicate that until the end of the cruise, when meltback was occurring in the southern part of the domain, the ice cover was typically between 90% and 100%. This raises the question: Does transformation of the NVWW occur away from large polynyas within smaller leads and openings? We note that there were many such small leads present in our study area, and most of the CTD stations occupied during the cruise were done in such openings (operationally, this was easier than making a hole in the pack-ice using the ship). Furthermore, in a large number of instances, these leads were actively refreezing. In general, leads can be open anywhere from hours to weeks (Smith et al., 1990). Brine rejection and salinization of the water column can continue even when

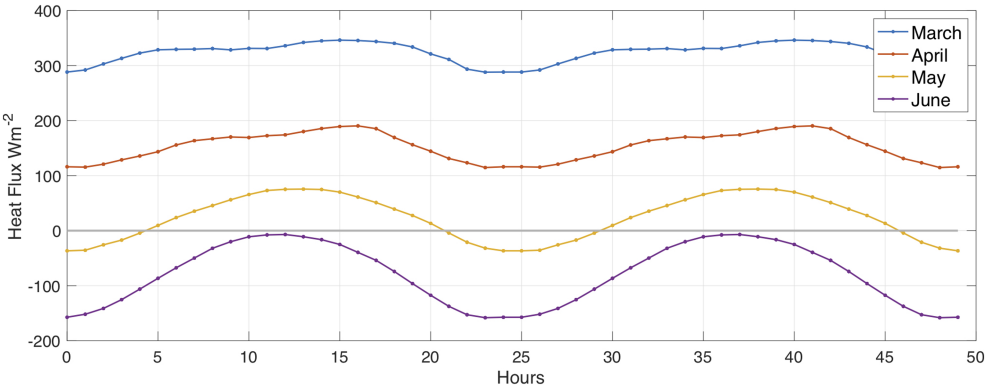

Figure 11. Monthly mean heat flux for March–June 2014 repeated over two diurnal cycles.

Table 1
Overturn Statistics for the Different Monthly Heat Flux Forcing Conditions

	March	April	May
Mean (hr)	13.6 ± 7.3	25.1 ± 11.3	35.3 ± 13.1
Minimum (hr)	0.5	0.67	0.67
24 hr vs. 48 hr (#)	168/179	76/169	5/24
Percent overturned (%)	99.4	93.9	13.3
Percent bottom–5 m (%)	99.4	95.0	22.6

Note. Bottom-5 m represents those profiles where convection reached 5 m above the bottom.

new ice has been formed in the lead (Smith et al., 1990). In the Chukchi Sea, leads tend to be 100 m or less in width, several kilometers in length, and oriented perpendicular to the prevailing wind; although the currents can play a role as well (Tschudi et al., 2002). The leads during this study were generally 50–200 m long (Lowry et al., 2018).

We now assess the likelihood that modification of winter water takes place broadly across the Chukchi shelf within the concentrated pack ice. Specifically, we seek to determine how readily the CTD profiles measured during our cruise might be homogenized via convective overturning in refreezing leads; that is, how quickly can the density jump between the surface and bottom mixed layers be eroded. Our approach is to use a polynya model, described in section 2.4, with a realistic air-sea heat loss to compute the salt flux to the surface layer during ice formation. This flux is subsequently used to drive a one-dimensional mixed layer model, outlined in section 2.5, with each CTD cast as an initial condition. The time it takes the water column to overturn is then tabulated for each site. While this exercise should be considered a thought experiment, we argue that based on the conditions noted above, it is likely that such overturning was happening during the first part of the cruise and in the months preceding it. While we do not have data during March and April, we operate under the assumption that the character of the leads was similar then, and that the hydrographic structure of the water column was comparable to that observed during the cruise (i.e., generally a two-layer structure).

As explained in section 2.2, we used the ERA5 hourly turbulent and radiative heat fluxes. Figure 10a shows a typical 24-hour period of the turbulent heat fluxes (sensible and latent) and net radiative fluxes for mid-May (we included a local time reference in the figure). There is a strong diurnal component in each of the heat flux terms. The net radiative flux switches sign from negative during the day (ocean heat gain due to short-wave radiation) to positive at night (ocean heat loss due to long wave radiation). Interestingly, the turbulent fluxes are out of phase with this: the largest sensible and latent heat losses occur during the day, and the smallest values occur at night. The reason for this is the diurnal cycle in wind, which is strongest during the day (Figure 10b). The air temperature is warmer during the day, but wind is the primary factor dictating the diurnal turbulent heat flux variation. Over the time period of the cruise, the total heat flux was positive at night until early June, at which point there was an abrupt reduction. After this, the flux remained mostly negative (or near zero) for the remainder of the sampling period.

We forced the PWP simulations with the monthly mean diurnal cycle in total heat flux for March, April, and May. These are shown in Figure 11, along with the month of June, which reveal the marked change in forcing from early spring to early summer. In March, the heat loss is nearly steady throughout the day and night, approximately 300 W/m^2. As spring progresses, the diurnal amplitude increases substantially, and the mean forcing over the 24-hr period decreases. By June, the heat flux is positive over the entire diurnal cycle. Thus, the role of the turbulent heat fluxes in driving convective overturning changes considerably through the season; in March, the turbulent heat loss dominates the forcing, while in May it helps moderate the radiative heating during the day.

At the start of each mixed layer calculation, we run the PWP model with the net heat flux until the surface temperature reaches the freezing point. This typically takes a few hours. After that, the polynya model is used to calculate the negative freshwater flux due to ice formation at each site. This assumes that, as the ice forms, it is continually advected out of the region by the ambient flow and by the wind (i.e., the same wind that opened up the ice in the first place). Finally, the calculated salt flux is used to force the PWP model. We considered two consecutive diurnal cycles of forcing for each run. The combined polynya-PWP model was applied to each of the CTD casts on the shelf that contained NVWW (181 stations).

The model results are tabulated in Table 1. In March, nearly all of the stations overturned in less than 24 hr, and the few remaining stations overturned during the second diurnal cycle. In April, roughly half of the stations overturned in less than 24 hr, and nearly all of them overturned within two diurnal cycles. By May, however, there was a substantial reduction in the amount of stations where convection reached the bottom, with 13% of the stations overturning after 2 days and less than 5% overturning after 1 day (see Table 1 for

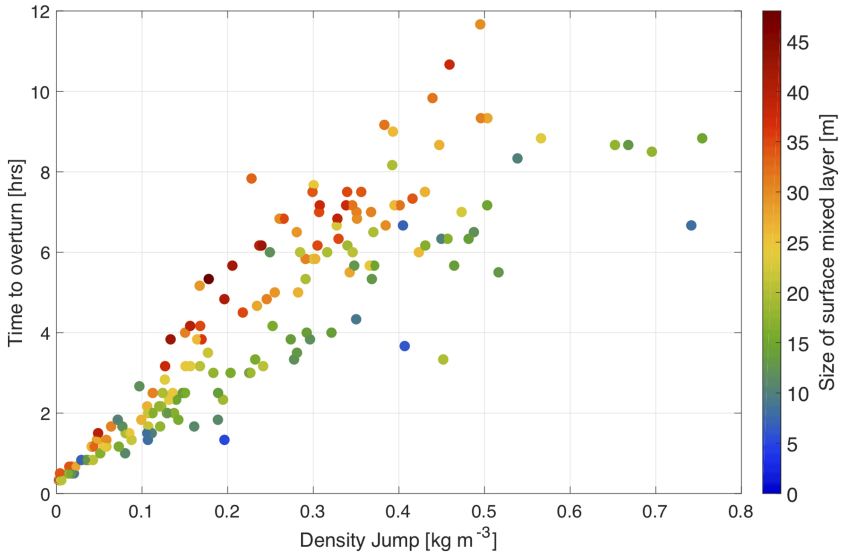

Figure 12. Relationship between overturn time and the density jump between the two mixed layers for the stations containing newly ventilated winter water, using the mean March heat flux. The color denotes the height of the surface mixed layer.

complete statistics). The mean overturn time corresponding to March forcing was 13.6 ± 7.3 hr, with a minimum time of only 30 min. In April, the mean overturn time was 25.1 ± 11.3 hr and in May, it increased to 35.3 ± 13.1 hr. These results imply that most of the profiles measured during the SUBICE cruise would have rapidly convected to the bottom if subjected to an open water lead during the months of March and April. By contrast, in May, only 24 stations overturned within 48 hr. This is consistent with the fact that relatively few of the CTD profiles (seven) measured during the cruise were neutrally stable. Additionally, only in May was there a notable difference in the percentage of stations convecting to within 5 m of the bottom versus all the way to the bottom. In particular, convection reaching 5 m above bottom (or into a slightly stratified bottom boundary layer) occurred 23% of the time in 48 hr, while convection reaching the bottom only occurred 13% of the time. Overall, we conclude that most of the northeast Chukchi shelf had been recently overturned and/or was poised for rapid overturning during the time of our survey.

It is of interest to understand what factors influence the overturn time. In doing so, we ignore the time that it takes to bring the surface temperature to the freezing point. The idea is to focus on the effect of the salt flux since, at these cold temperatures, salinity dictates the density; and hence, the convective overturning. Figure 12 shows the overturn time, once ice starts to form, regressed against the magnitude of the density jump of the profile for March forcing. There is a clear correlation in that larger density jumps correspond to longer overturn times. This is not surprising since it takes more energy to overcome a stronger interface and bring the surface mixed layer to the density of the bottom mixed layer. However, as is evident from the figure, for larger values of the density jump, there is more scatter in how long the water column takes to overturn. To explain this, we considered the thickness of the surface mixed layer, which is indicated by color in Figure 12. One sees that for a given density jump, the thicker the layer the longer it takes to overturn the water column. This is again reasonable, as the effect of a given salinity increase from brine rejection will be smaller if the mixed-layer is larger, since the brine must mix with more water and will therefore increase the overall density of the surface mixed layer less than if the layer were thinner.

To quantify this further, we defined a "barrier" parameter b = (density jump) × (thickness of the surface mixed layer), which takes into account both of these characteristics of the profile. This parameter was calculated for each station and compared to the overturn time given by the coupled model (Figure 13), revealing a clear linear relationship ($r = 0.92$). It is therefore evident that, once ice starts to form, the time it takes a two-layer profile to completely mix is dictated by two factors: the thickness of the surface mixed layer and the size of the density jump. This provides a means to better understand which profiles are poised to overturn the fastest and the time scales associated with the homogenization of the water column.

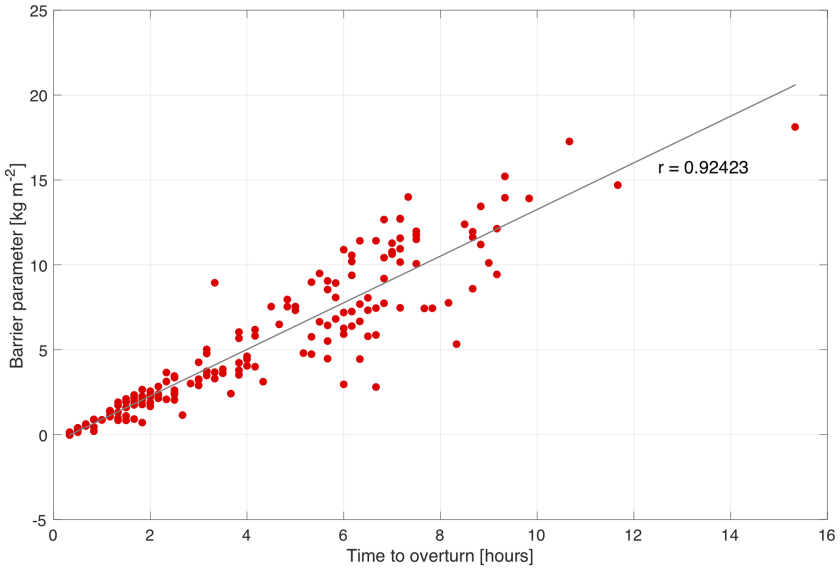

Figure 13. Relationship between overturn time and the value of the barrier parameter *b* for the stations containing newly ventilated winter water, using the mean March heat flux. See text for details.

3.2.3. Transformation by Polynyas Versus Small Leads

It has been previously documented that NVWW can be transformed in large polynyas (Gong & Pickart, 2016; Itoh et al., 2012; Pickart et al., 2016; Weingartner et al., 1998). The results presented above indicate that the stations on the shelf during our survey were poised for rapid overturning and/or had recently overturned. Furthermore, we sampled seven profiles that were homogenized to within 0.01 kg/m^3 in a region of heavy ice cover, with only small leads and openings in the sea ice. This strongly suggests that NVWW is modified outside of large polynyas. The next question is, is the degree of such transformation comparable to that which occurs in polynyas? To assess this, we compared the salinity of the NVWW measured during our cruise along the central flow pathway to that recorded by moorings earlier in the year in Bering Strait in order to determine if salinization took place on the shelf—and, if so, to see if this could be explained solely by polynya activity or whether salinization within leads was needed as a mechanism for elevated salinity values.

We used the same approach as that employed by Pickart et al. (2016) in their investigation of winter water transformation on the Chukchi shelf. First, we identified the stations along the central flow pathway, that is, the branch that extends around the north side of Hanna Shoal (Figure 9). The average salinity of the NVWW in both the surface and bottom mixed layers for the parts of the five transects that crossed the pathway reveals a marked decrease progressing northwards. Using an average advective speed of 9.2 cm/s, we traced these parcels back in time to when they would have passed through Bering Strait, and compared the bottom mixed layer salinities to the salinity timeseries at mooring A3 at a 44-m depth in the strait (the location of the mooring is marked in Figure 14). We tried a range of advective speeds, and a value of 9.2 cm/s resulted in the most sensible results in terms of the relationship between the shipboard hydrographic data and the mooring record. We note that this average speed inherently includes any instances of flow reversals within polynyas (given that polynyas are driven by northerly and northeasterly winds (Kawaguchi et al., 2011) in this region). In light of the ADCP flow speeds (Figure 9) and their uncertainty (see section 2.1), such a value is reasonable (also keep in mind the large distance from Bering Strait to the CC line for which we have no velocity measurements). This is also close to the optimal advective speed of 10.5 cm/s determined in the same way by Pickart et al. (2016) for the same pathway.

Our results indicate that the salinities at the three northern transects match the Bering Strait timeseries, but the values at the two southern transects are saltier by ~0.35. To determine if this difference can be explained by salinization within polynyas, we used the daily AMSR-2 satellite product to document the ice concentration following five parcels leaving Bering Strait between late February and early April and traveling northward through the Central Channel. The five parcels in question are those that would end up at the five

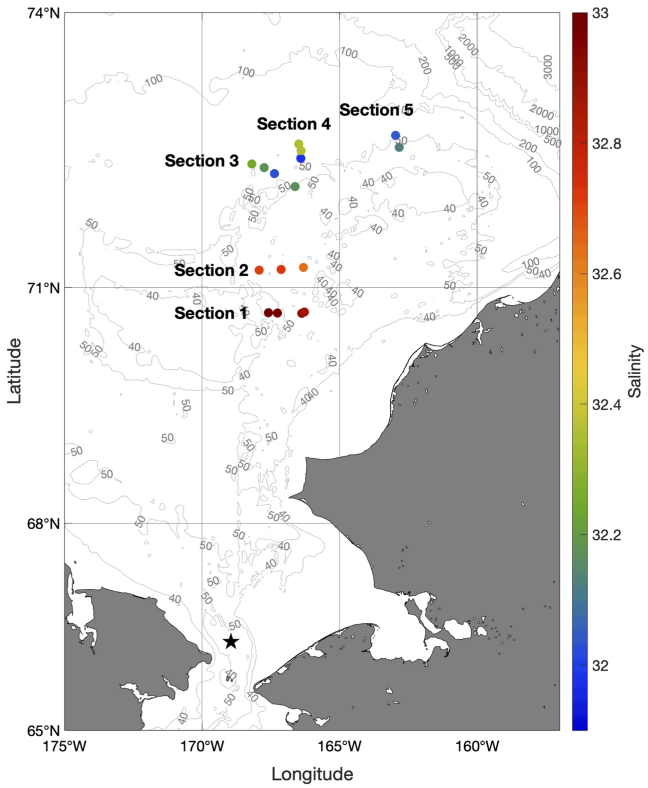

Figure 14. Average salinity (color) of the bottom mixed layer for the stations along the central flow pathway. The location of the Bering Strait mooring A3 is denoted by the black star.

locations, respectively, in the central pathway (Figure 14) at the time of sampling of the given transect, based on the advective speed of 9.2 cm/s. This revealed that the first four parcels encountered heavy ice concentration, greater than 80% and mostly between 90% and 100% (except for a brief period at the beginning of the record, Figure 15). Only the final parcel—the one sampled at transect 2—passed through a polynya. In particular, it encountered the southwestern end of the northeast Chukchi polynya twice in May before reaching its sampling point (corresponding to the large reductions in ice concentration in Figure 15).

Using a data set collected in 2011, Pickart et al. (2016) determined that NVWW traveling along the central pathway was salinized within the northeast Chukchi polynya. They used the same polynya model as that employed above to estimate the brine rejection following parcels along the pathway, and found that the predicted salinity increase between Bering Strait and the measurement locations on the shelf was sufficient to explain the observed changes. We use the same methodology here on the final parcel which passed through the northeast Chukchi polynya. Following Pickart et al. (2016), we assume that the parcel is at the freezing point and then calculate the salinization each day that the parcel experiences ice concentrations below 80%. We use the corresponding monthly mean heat flux (322 W/m^2 for March, 153 W/m^2 for April, 23 W/m^2 for May, and −80 W/m^2 for June). The result indicates that the salinity of this parcel is increased by 0.05, which is far less than the observed increase of 0.35. This result is not sensitive to the choice of ice concentration required for salinization. Values of 85%, 90%, and 95% generate salinity increases of 0.05, 0.10, and 0.17, respectively, still well below the observed change. Furthermore, the increase in salinity at transect 1 in Figure 15, which was 0.48, cannot be explained by polynya activity since the water in question did not encounter any polynyas during the transit from Bering Strait to the measurement location (even when polynya activity is defined by 95% ice concentration, the salinity increase of transect 1 cannot be described by polynya activity). This implies that salinization within small leads in consolidated pack ice can be as effective, or more so, as that occurring in larger polynyas.

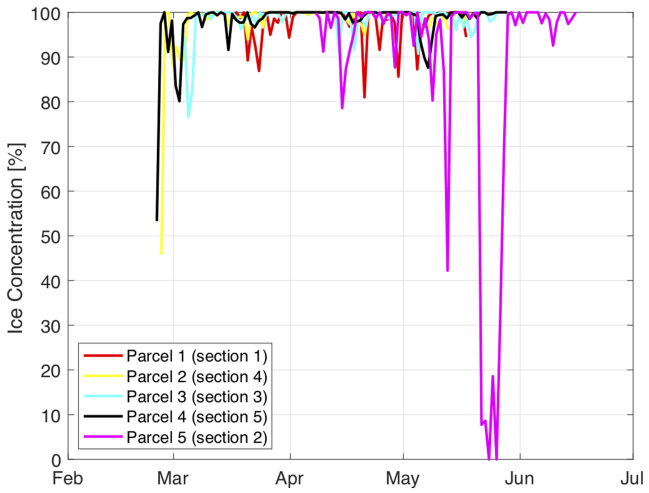

Figure 15. Ice concentration from AMSR-2 following each of the five parcels emanating from Bering Strait (see text for details).

3.2.4. Ramifications for Primary Production

It is evident then that during the cold season, whenever a narrow lead in the ice opens up, it does not take much for convection to erode the weak stratification and reach the bottom. Importantly, when this happens, the nutrients in and above the sediments will be stirred into the upper water column (see Cooper et al., 1997). These nutrient-enhanced waters have been shown to be laterally exported off the Chukchi Shelf and to ventilate the Arctic Ocean nutricline (Jones & Anderson, 1986; Moore et al., 1983). Vertical export of carbon is strong in the Chukchi Sea since the zooplankton are not able to consume all of the primary production that occurs each summer (Campbell et al., 2009). The remaining organic matter sinks to the seafloor where it is remineralized, both by microbial activity and cycling by the benthic macrofauna, resulting in high levels of inorganic nutrients in the pore water (Mathis et al., 2014). Hence, the convection on the Chukchi shelf during the cold season is able to tap these nutrients and transport them to the surface layer where they are available for primary production the following spring and summer. Similarly, analysis of chemical data from the same hydrographic survey showed elevated concentrations of trace metals (particularly Fe and Mn) stirred from the benthos (Vieira et al., 2019), providing further evidence of active convection bringing sediment properties into the upper water column.

This local source of nutrients, together with the remote supply advected through Bering Strait, is apparently enough to fill most of the Chukchi Sea with high concentrations of nitrate (which is the limiting nutrient for primary production on the shelf; Codispoti et al., 2005). The more active the convection, the saltier the water will be and the more sustained the vertical transport of nitrate will be. This is consistent with the high correlation between these two variables seen in our data set (discussed as well in Arrigo et al., 2017). When the ice cover first forms in late fall or early winter on the Chukchi shelf, brine-driven convection likely occurs. We are suggesting that continued convection in leads throughout the winter and spring would provide a more continual supply of nutrients. This emphasizes the importance of a dynamic ice pack (i.e., lots of openings) and the fact that the Chukchi Sea is shallow (i.e., the ability for convection to reach the bottom) for the seasonal occurrence of phytoplankton blooms throughout the shelf.

4. Summary

We have presented data from a broad-scale hydrographic survey of the Chukchi Sea carried out in late spring 2014. The measurement domain covered much of the northeast shelf, and more than 96% of the water sampled on the shelf was newly ventilated winter water. Nearly all of the hydrographic profiles sampled on the shelf consisted of a two-layer structure, with a surface mixed layer and bottom boundary layer separated by a weak density interface. The saltiest (densest) NVWW tended to be in the flow pathways on the shelf, likely advected there from the Bering Sea where winter water is known to be formed. However, away from the pathways, the NVWW was also found in abundance, suggesting that the entire Chukchi Sea is filled with winter water at the end of the cold season.

The fact that NVWW was found in regions of highly consolidated pack-ice, outside of the flow pathways and away from known polynyas, suggests a new paradigm for the formation/transformation of this water mass. We argue that winter water is formed throughout the Chukchi shelf via convection within small leads and openings. Our study domain was filled with such small leads—many of them refreezing—and we sampled profiles with a uniform density structure from top to bottom. Using the output of a polynya model to drive a one-dimensional mixing model, we demonstrated that, on average, the profiles would become completely homogenized within 14–25 hr when subjected to the March and April heat fluxes, and a subset of these profiles would become homogenized when subjected to the May heat fluxes. We also showed that the salinity signals of the NVWW along the central shelf pathway could not be explained solely by advection from Bering Strait or via modification within large polynyas. These results reinforce our assertion that convection in leads is an important mechanism forming NVWW on the Chukchi shelf.

When convection reaches the bottom, regenerated nutrients from the sediments are stirred into the water column. This can explain the fact that nitrate concentrations were high throughout our study domain. It is also consistent with the statistically significant correlation between the salinity of NVWW and its nitrate concentration, the idea being that continued brine rejection increases the convective activity, which is more effective for fluxing nutrients upwards from the bottom. Therefore, the presence of narrow leads in the ice, together with the fact that the Chukchi Sea is generally shallow, could contribute significantly to the high level of primary production on the shelf—so long as there is significant vertical export of organic matter to the sea floor following the annual summer blooms. As discussed previously, NVWW is known to ventilate the halocline of the Canada Basin. Given that this vintage of NVWW is continuously salinized along its trajectory northward, it will be denser than the winter water advected through Bering Strait. Thus, its equilibrium depth in the basin will be deeper. This in turn makes it possible to imprint the enhanced nitrate signature within a deeper portion of the Arctic halocline.

Despite the favorable "initial condition" of high nitrate in the surface water throughout our study domain, no significant under-ice blooms were observed during the 6-week cruise. We attribute this to the fact that melt ponds did not develop during our measurement period, which meant that there was not enough light in the water column. Further work is required to determine the reasons for the minimal melt pond activity, and what role the atmospheric forcing played. In any event, it demonstrates that the nutrient distributions alone do not dictate the development of under-ice blooms in the Chukchi Sea.

Acknowledgments
The authors are indebted to Commanding Officer John Reeves, Executive Officer Gregory Stanclik, Operations Officer Jacob Cass, and the entire crew of the USCGC *Healy* for their hard work and dedication in making the SUBICE cruise a success. We also acknowledge Scott Hiller for his assistance with *Healy*'s meteorological data. We thank an anonymous reviewer for helpful input that improved the paper. Funding for A. P., R. P., C. N., and F. B. was provided by the National Science Foundation (NSF) under grant PLR-1303617. K. M. was funded by the Natural Sciences and Engineering Research Council of Canada. K. V. acknowledges the Bergen Research Foundation under Grant BFS2016REK01. K. A. was supported by the NSF grant PLR-1304563. The CTD and shipboard ADCP data are available from https://www.rvdata.us/search/cruise/HLY1401, and the nutrient data can be accessed from https://arcticdata.io/catalog/view/doi:10.18739/A2RG3Z and http://ocean.stanford.edu/subice/. The shipboard meteorological data reside at http://ocean.stanford.edu/subice/.

References

Aagaard, K. (1984). The Beaufort undercurrent. In P. W. Barnes, D. M. Schell, & E. Reimnitz (Eds.), *The Alaskan Beaufort Sea*, (pp. 47–71). San Diego, Calif: Academic.

Aagaard, K., & Roach, A. T. (1990). Arctic Ocean-shelf exchange: Measurements in Barrow Canyon. *Journal of Geophysical Research*, *95*(C10), 18163–18175. https://doi.org/10.1029/JC095iC10p18163

Aksenov, Y., Ivanov, V. V., Nurser, A. J. G., Bacon, S., Polyakov, I. V., Coward, A. C., et al. (2011). The arctic circumpolar boundarycurrent. *Journal of Geophysical Research*, *116*, C09017. https://doi.org/10.1029/2010JC006637

Armstrong, F., Stearns, C. R., & Strickland, J. (1967). The measurement of upwelling and subsequent biological process by means of the TechniconAutoanalyzer® and associated equipment. *Deep Sea Research and Oceanographic Abstracts*, *14*(3), 381–389. https://doi.org/10.1016/0011-7471(67)90082-4

Arrigo, K. R., Mills, M. M., van Dijken, G. L., Lowry, K. E., Pickart, R. S., & Schlitzer, R. (2017). Late spring nitrate distributions beneath the ice-covered Chukchi shelf. *Journal of Geophysical Research: Biogeosciences*, *122*, 2409–2417. https://doi.org/10.1002/2017JG003881

Arrigo, K. R., Perovich, D. K., Pickart, R. S., Brown, Z. W., van Dijken, G. L., Lowry, K. E., et al. (2012). Massive phytoplankton blooms under Arctic sea ice. *Science*, *336*(6087), 1408. https://doi.org/10.1126/science.1215065

Arrigo, K. R., Perovich, D. K., Pickart, R. S., Brown, Z. W., van Dijken, G. L., Lowry, K. E., et al. (2014). Phytoplankton blooms beneath the sea ice in the Chukchi Sea. *Deep Sea Research Part II: Topical Studies in Oceanography*, *105*, 1–16. https://doi.org/10.1016/j.dsr2.2014.03.018

Beitsch, A., Kaleschke, L., & Kern, S. (2014). Investigating high-resolution AMSR2 sea ice concentrations during the February 2013 fracture event in the Beaufort Sea. *Remote Sensing*, *6*(5), 3841–3856. https://doi.org/10.3390/rs6053841

Bourke, R. H., & Paquette, R. G. (1976). Atlantic water on the Chukchi Shelf. *Geophysical Research Letters*, *3*(10), 629–632. https://doi.org/10.1029/GL003i010p00629

Campbell, R. G., Sherr, E. B., Ashjian, C. J., Plourde, S., Sherr, B. F., Hill, V., & Stockwell, D. A. (2009). Mesozooplankton prey preference and grazing impact in the Western Arctic Ocean. *Deep Sea Research Part II: Topical Studies in Oceanography*, *56*(17), 1274–1289. https://doi.org/10.1016/j.dsr2.2008.10.027

Cavalieri, D. J., & Martin, S. (1994). The contribution of Alaskan, Siberian, and Canadian coastal polynyas to the cold halocline of the Arctic Ocean. *Journal of Geophysical Research*, *99*(C9), 18343–18362. https://doi.org/10.1029/94JC01169

Chauduri, A. H., Ponte, R. M., & Nguyen, A. T. (2014). A comparison of atmospheric reanalysis products for the Arctic Ocean and implications for uncertainties in air-sea fluxes. *Journal of Climate*, *27*(14), 5411–5421. https://doi.org/10.1175/JCLI-D-13-00424.1

Codispoti, L. A., Flagg, C., Kelly, V., & Swift, J. H. (2005). Hydrographic conditions during the 2002 SBI process experiments. *Deep Sea Research Part II: Topical Studies in Oceanography*, *52*(24-26), 3199–3226.

Cooper, L. W., Whitledge, T. E., Grebmeier, J. M., & Weingartner, T. J. (1997). The nutrient, salinity, and stable oxygen isotope composition of Bering and Chukchi Seas waters in and near the Bering Strait. *Journal of Geophysical Research*, *102*(C6), 12563–12573. https://doi.org/10.1029/97JC00015

Corlett, W. B., & Pickart, R. S. (2017). The Chukchi slope current. *Progress in Oceanography*, *153*, 50–65. https://doi.org/10.1016/j.pocean.2017.04.005

Gong, D., & Pickart, R. S. (2015). Summertime circulation in the eastern Chukchi Sea. *Deep Sea Research Part II: Topical Studies in Oceanography*, *118*, 18–31. https://doi.org/10.1016/j.dsr2.2015.02.006

Gong, D., & Pickart, R. S. (2016). Early summer water mass transformation in the eastern Chukchi Sea. *Deep Sea Research Part II: Topical Studies in Oceanography*, *130*, 43–55. https://doi.org/10.1016/j.dsr2.2016.04.015

Hersbach, H., & Dee, D. (2016). ERA5 reanalysis is in production. In *ECMWF Newsletter*, (Vol. 147, p. 7). Reading, UK: ECMWF.

Hill, V., & Cota, G. (2005). Spatial patterns of primary production in the Chukchi Sea in the spring and summer of 2002. *Deep Sea Research Part II: Topical Studies in Oceangoraphy*, *52*(24-26), 3344–3354. https://doi.org/10.1016/j.dsr2.2005.10.001

Itoh, M., Pickart, R. S., Kikuchi, T., Fukamachi, Y., Ohshima, K. I., Simizu, D., et al. (2015). Water properties, heat and volume fluxes of Pacific water in Barrow Canyon during summer 2010. *Deep Sea Research Part I: Oceanographic Research Papers*, *102*(c), 43–54. https://doi.org/10.1016/j.dsr.2015.04.004

Itoh, M., Shimada, K., Kamoshida, T., McLaughlin, F., Carmack, E. C., & Nishino, S. (2012). Interannual variability of Pacific winter water inflow through Barrow Canyon from 2000 to 2006. *Journal of Oceanography*, *68*(4), 575–592. https://doi.org/10.1007/s10872-012-0120-1

Jones, E. P., & Anderson, L. G. (1986). On the origin of the chemical properties of the Arctic Ocean halocline. *Journal of Geophysical Research*, *91*(C9), 10759–10767. https://doi.org/10.1029/JC091iC09p10759

Karcher, M., Kauker, F., Gerdes, R., Hunke, E., & Zhang, J. (2007). On the dynamics of Atlantic Water circulation in the Arctic Ocean. *Journal of Geophysical Research*, *112*, C04S02. https://doi.org/10.1029/2006JC003630

Kawaguchi, Y., Tamura, T., Nishino, S., Kikuchi, T., Itoh, M., & Mitsudera, H. (2011). Numerical study of winter water formation in the Chukchi Sea: Roles and impacts of coastal polynyas. *Journal of Geophysical Research*, *116*, C07025. https://doi.org/10.1029/2010JC006606

Ladd, C., Mordy, C. W., Salo, S. A., & Stabeno, P. J. (2016). Winter water properties and the Chukchi Polynya. *Journal of Geophysical Research: Oceans*, *121*, 5516–5534. https://doi.org/10.1002/2016JC011918

Lentz, S., & Trowbridge, J. (1991). The bottom boundary layer over the northern Californian Shelf. *Journal of Physical Oceanography*, *21*(8), 1186–1201. https://doi.org/10.1175/1520-0485(1991)021<1186:TBBLOT>2.0.CO;2

Li, M., Pickart, R. S., Spall, M. A., Weingartner, T. J., Lin, P., Moore, G. W. K., & Qi, Y. (2019). Circulation of the Chukchi shelfbreak and slope from moored timeseries. *Progress in Oceanography*, *172*, 14–33. https://doi.org/10.1016/j.pocean.2019.01.002

Lin, P., Pickart, R. S., McRaven, L. T., Arrigo, K. R., Bahr, F., Lowry, K. E., et al. (2019). Water mass evolution and circulation of the northeastern Chukchi Sea in summer: Implications for nutrient distributions. *Journal of Geophysical Research: Oceans*, *124*, 4416–4432. https://doi.org/10.1029/2019JC015185

Lindsay, R., Wensnahan, M., Schweiger, A., & Zhang, J. (2014). Evaluation of Seven Different Atmospheric Reanalysis Products in the Arctic. *Journal of Climate*, *27*(7), 2588–2606. https://doi.org/10.1175/JCLI-D-13-00014.1

Lowry, K. E., Pickart, R. S., Mills, M. M., Brown, Z. W., van Dijken, G. L., Bates, N. R., & Arrigo, K. R. (2015). Influence of winter water on phytoplankton blooms in the Chukchi Sea. *Deep Sea Research Part II: Topical Studies in Oceanography*, *118*, 53–72. https://doi.org/10.1016/j.dsr2.2015.06.006

Lowry, K. E., Pickart, R. S., Mills, M. M., Pacini, A., Selz, V., & Lewis, K. M. (2018). Under-ice phytoplankton blooms inhibited by spring convective mixing in refreezing leads. *Journal of Geophysical Research: Oceans*, *123*, 90–109. https://doi.org/10.1002/2016JC012575

Lowry, K. E., van Dijken, G. L., & Arrigo, K. R. (2014). Evidence of under-ice phytoplankton blooms in the Chukchi Sea from 1998 to 2012. *Deep Sea Research Part II: Topical Studies in Oceanography*, *105*, 105–117. https://doi.org/10.1016/j.dsr2.2014.03.013

Mathis, J.T., Grebmeier, J.M., Hansell, D.A., Hopcroft, R.R., Kirchman, D., Lee, S.H., et al. (Eds.), *The Pacific Arctic Region: Ecosystem Status and Trends in a Rapidly Changing Environment*, Springer, Dordrecht, p. 223-268.

Mathis, J. T., Pickart, R. S., Hansell, D. A., Kadko, D., & Bates, N. R. (2007). Eddy transport of organic carbon and nutrients from the Chukchi Shelf: Impact on the upper halocline of the western Arctic Ocean. *Journal of Geophysical Research*, *112*, C05011. https://doi.org/10.1029/2006JC003899

Moore, R. M., Lowings, M. G., & Tan, F. C. (1983). Geochemical profiles in the central Arctic Ocean: Their relationship to freezing and shallow circulation. *Journal of Geophysical Research*, *88*(C4), 2667–2674. https://doi.org/10.1029/JC088iC04p02667

Muench, R. D., Schumacher, J. D., & Salo, S. A. (1988). Winter currents and hydrographic conditions on the northern central Bering Sea shelf. *Journal of Geophysical Research*, *93*(C1), 516–526. https://doi.org/10.1029/JC093iC01p00516

Padman, L., & Erofeeva, S. (2004). A barotropic inverse tidal model for the Arctic Ocean. *Geophysical Research Letters*, *31*, L02303. https://doi.org/10.1029/2003GL019003

Paquette, R. G., & Bourke, R. H. (1974). Observation on the coastal current of Arctic Alaska. *Journal of Marine Research*, *32*, 195–207.

Petersen, G. N., & Renfrew, I. A. (2009). Aircraft-based observations of air-sea fluxes over Denmark Strait and the Irminger Sea during high wind speed conditions. *Quarterly Journal of the Royal Meteorological Society*, *135*(645), 2030–2045. https://doi.org/10.1002/qj.355

Pickart, R. S., Moore, G. W. K., Mao, C., Bahr, F., Nobre, C., & Weingartner, T. J. (2016). Circulation of winter water on the Chukchi shelf in early summer. *Deep Sea Research Part II: Topical Studies in Oceanography*, *130*, 56–75. https://doi.org/10.1016/j.dsr2.2016.05.001

Pickart, R. S., Nobre, C., Lin, P., Arrigo, K. R., Ashjian, C. J., Berchok, C., et al. (2019). Seasonal to mesoscale variability of water masses and atmospheric conditions in Barrow Canyon, Chukchi Sea. *Deep Sea Research Part II: Topical Studies in Oceanography*, *162*, 32–49. https://doi.org/10.1016/j.dsr2.2019.02.003

Pickart, R. S., Pratt, L. J., Torres, D. J., Whitledge, T. E., Proshutinsky, A. Y., Aagaard, K., et al. (2010). Evolution and dynamics of the flow through Herald Canyon in the western Chukchi Sea. *Deep Sea Research Part II: Topical Studies in Oceanography*, *57*(1–2), 5–26. https://doi.org/10.1016/j.dsr2.2009.08.002

Pickart, R. S., Torres, D. J., & Clarke, R. A. (2002). Hydrography of the Labrador Sea during active convection. *Journal of Physical Oceanography*, *32*(2), 428–457. https://doi.org/10.1175/1520-0485(2002)032<0428:HOTLSD>2.0.CO;2

Pickart, R. S., Weingartner, T. J., Pratt, L. J., Zimmermann, S., & Torres, D. J. (2005). Flow of winter-transformed Pacific water into the Western Arctic. *Deep Sea Research Part II: Topical Studies in Oceanography*, *52*(24–26), 3175–3198. https://doi.org/10.1016/j.dsr2.2005.10.009

Pisareva, M. N., Pickart, R. S., Lin, P., Fratantoni, P. S., & Weingartner, T. J. (2019). On the nature of wind-forced upwelling in Barrow Canyon. *Deep Sea Research Part II: Topical Studies in Oceanography*, *162*, 63–78. https://doi.org/10.1016/j.dsr2.2019.02.002

Pisareva, M. N., Pickart, R. S., Spall, M. A., Nobre, C., Torres, D. J., Moore, G. W. K., & Whitledge, T. E. (2015). Flow of Pacific water in the western Chukchi Sea: Results from the 2009 RUSALCA expedition. *Deep Sea Research Part I: Oceanographic Research Papers*, *105*, 53–73. https://doi.org/10.1016/j.dsr.2015.08.011

Price, J. F., Weller, R. A., & Pinkel, R. (1986). Diurnal cycling: Observations and models of the upper ocean response to diurnal heating, cooling and wind mixing. *Journal of Geophysical Research*, *91*(C7), 8411–8427. https://doi.org/10.1029/JC091iC07p08411

Renfrew, I. A., Moore, G. W. K., Guest, P. S., & Bumke, K. (2002). A comparison of surface layer and surface turbulent flux observations over the Labrador Sea with ECMWF analyses and NCEP reanalyses. *Journal of Physical Oceanography*, *32*, 383–400. https://doi.org/10.1175/1520-0485(2002)032<0383:ACOSLA>2.0.CO;2

Rudels, B., Jones, E. P., Schauer, U., & Eriksson, P. (2004). Atlantic sources of the Arctic Ocean surface and halocline waters. *Polar Research*, *23*, 181–208. https://doi.org/10.1111/j.1751-8369.2004.tb00007.x

Shimada, K., Carmack, E. C., Hatakeyama, K., & Takizawa, T. (2001). Varieties of shallow temperature maximum waters in the western Canadian basin of the Arctic Ocean. *Geophysical Research Letters*, *28*, 3441–3444. https://doi.org/10.1029/2001GL013168

Smith, S. D., Muench, R. D., & Pease, C. H. (1990). Polynyas and leads: An overview of physical processes and environment. *Journal of Geophysical Research*, *95*(C6), 9461–9479. https://doi.org/10.1029/JC095iC06p09461

Spall, M. A., Pickart, R. S., Fratantoni, P. S., & Plueddemann, A. J. (2008). Western Arctic shelfbreak eddies: Formation and transport. *Journal of Physical Oceanography*, *38*, 1644–1668. https://doi.org/10.1175/2007JPO3829.1

Steele, M., Morison, J., Ermold, W., Rigor, I., Ortmeyer, M., & Shimada, K. (2004). Circulation of summer Pacific halocline water in the Arctic Ocean. *Journal of Geophysical Research*, *109*, C02027. https://doi.org/10.1029/2003JC002009

Timmermans, M.-L., Toole, J., Proshutinsky, A., Krishfield, R., & Plueddemann, A. (2008). Eddies in the Canada Basin, Arctic Ocean, observed from ice-tethered profilers. *Journal of Physical Oceanography*, *38*, 133–145. https://doi.org/10.1175/2007JPO3782.1

Trowbridge, J. H., & Lentz, S. J. (1991). Asymmetric behavior of an oceanic boundary layer above a sloping bottom. *Journal of Physical Oceanography*, *21*, 1171–1185. https://doi.org/10.1175/1520-0485(1991)021<1171:ABOAOB>2.0.CO;2

Tschudi, M. A., Curry, J. A., & Maslanik, J. A. (2002). Characterization of springtime leads in the Beaufort/Chukchi Seas from airborne and satellite observations during FIRE/SCHEBA. *Journal of Geophysical Research*, *107*(C10), 8034. https://doi.org/10.1029/2000JC000541

Vieira, L. H., Achterberg, E., Scholten, J., Beck, A. J., Liebetrau, V., Mills, M. M., & Arrigo, K. R. (2019). Benthic fluxes of trace metals in the Chukchi Sea and their transport into the Arctic Ocean. *Marine Chemistry*, *208*, 43–55. https://doi.org/10.1016/j.marchem.2018.11.001

von Appen, W.-J., & Pickart, R. S. (2012). Two configurations of the western Arctic shelfbreak current in summer. *Journal of Physical Oceanography*, *42*(3), 329–351. https://doi.org/10.1175/JPO-D-11-026.1

Walsh, J. E., Chapman, W. L., & Portis, D. H. (2009). Arctic cloud fraction and radiative fluxes in atmospheric reanalyses. *Journal of Climate*, *22*, 2316–2334. https://doi.org/10.1175/2008JCLI2213.1

Weingartner, T., Aagaard, K., Woodgate, R., Danielson, S., Sasaki, Y., & Cavalieri, D. (2005). Circulation on the north central Chukchi Sea shelf. *Deep Sea Research Part II: Topical Studies in Oceanography*, *52*(24–26), 3150–3174. https://doi.org/10.1016/j.dsr2.2005.10.015

Weingartner, T., Danielson, S., Sasaki, Y., Pavlov, V., & Kulakov, M. (1999). The Siberian Coastal current: A wind- and buoyancy-forced Arctic coastal current. *Journal of Geophysical Research*, *104*(C12), 29,697–29,713. https://doi.org/10.1029/1999JC900161

Weingartner, T. J., Cavalieri, D. J., Aagaard, K., & Sasaki, Y. (1998). Circulation, dense water formation, and outflow on the northeast Chukchi shelf. *Journal of Geophysical Research*, *103*(C4), 7647–7661. https://doi.org/10.1029/98JC00374

Woodgate, R. A., Aagaard, K., & Weingartner, T. J. (2005). A year in the physical oceanography of the Chukchi Sea: Moored measurements from autumn 1990–1991. *Deep Sea Research Part II: Topical Studies in Oceanography*, *52*(24–26), 3116–3149. https://doi.org/10.1016/j.dsr2.2005.10.016

Zhao, M., Timmermans, M.-L., Cole, S., Krishfield, R., Proshutinsky, A., & Toole, J. (2014). Characterizing the eddy field in the Arctic Ocean halocline. *Journal of Geophysical Research: Oceans*, *119*, 8800–8817. https://doi.org/10.1002/2014JC010488

Zhao, M., Timmermans, M.-L., Cole, S., Krishfield, R., & Toole, J. (2016). Evolution of the eddy field in the Arctic Ocean's Canada Basin, 2005-2015. *Geophysical Research Letters*, *43*, 8106–8114. https://doi.org/10.1002/2016GL069671